Hindawi
International Journal of Aerospace Engineering
Volume 2023, Article ID 3304048, 25 pages
https://doi.org/10.1155/2023/3304048

Research Article

Aerodynamic Analysis of a Logistics UAV with Foldable Bi-wing Configuration

Xiaolu Wang,[1] **Wenlong Lu**,[1] **Weiwei Liu**,[1] **Changning Chen**,[1] **and Liangyu Zhao**[2]

[1]*School of Aerospace Engineering, Zhengzhou University of Aeronautics, Zhengzhou 450046, China*
[2]*School of Aerospace Engineering, Beijing Institute of Technology, Beijing 100081, China*

Correspondence should be addressed to Xiaolu Wang; wangxl@zua.edu.cn

Received 29 August 2023; Revised 7 November 2023; Accepted 10 November 2023; Published 5 December 2023

Academic Editor: Alex Zanotti

Herein, a twin-boom, inverted V-tailed unmanned aerial vehicle (UAV) featuring a foldable bi-wing configuration is proposed for logistics and transportation applications. We employed the Navier–Stokes solver to numerically simulate steady, incompressible flow conditions. By examining the effects of key design parameters on aerodynamic characteristics and bypass flow fields in a two-dimensional state, we were able to suggest a more optimized foldable wing design. Building on the two-dimensional analysis, we performed aerodynamic assessments of the three-dimensional aircraft geometry. Our results indicated that appropriate wing and gap parameters can significantly enhance lift characteristics, maintaining high lift even during large-angle flights. Specifically, when compared to a mono-wing, the lift coefficient of the bi-wing increased by 27.1% at a 14° angle of attack, demonstrating the effectiveness of our wing-and-gap design. Optimal aerodynamic performance was achieved when the gap distance equalled the chord length in both flow and vertical directions. Further, the right combination of airfoil configuration, wing axes angle, and wingspan can improve flow field aerodynamic characteristics, while also enhancing the wing's stall capacity. The lift coefficient reached its maximum value at an angle of attack of 15°, which has the potential to reduce takeoff and landing distances, thereby enhancing the UAV's overall safety.

1. Introduction

Given the advancements in general aviation technology and improvements in logistics efficiency, there has been a consistent rise in demand for faster and larger load-carrying capabilities in the logistics and transportation sectors [1]. While land and air cargo transport have gained traction, the cost and efficiency of transporting goods in mountainous, plateau, and island regions remain a challenge. Unmanned aerial vehicles (UAVs) have emerged as a promising solution, offering quicker transport times and reduced labour costs [2–6]. Reports by Szalanczi-Orban and Vaczi show that the global drone market is on an upward trajectory, demonstrating ever-increasing growth and economic potential [7]. According to Kapustina et al., the global drone market is expected to grow from $20 billion to $45 billion by 2025, cementing drones as a burgeoning application area in logistics [8]. Given their technology-intensive nature, drones are poised to have a significant positive impact on the market. Research by Merkert et al. indicates that, all things being equal, people generally prefer traditional postal delivery, but drones could gain substantial market share if they offer quicker and more cost-effective options [9].

In comparison to motorized transport, traditional UAVs often require fixed runways for takeoff and landing. This presents challenges in constructing long enough runways in areas such as mountains or hills. Tilt-rotor aircraft, while innovative, tend to underperform fixed-wing UAVs in aspects like equipment weight, aerodynamic efficiency, and energy consumption. The payload limitations of these UAVs also reduce their efficiency per transport. In contrast, fixed-wing aircraft, known for their superior aerodynamic performance, are generally used for heavy cargo transport. To be viable for logistics, these UAVs must possess sufficient takeoff lift and short takeoff and landing (STOL) capabilities, all while minimizing aerodynamic losses during cruising. This has become a key research direction in the field of logistics-focused UAVs.

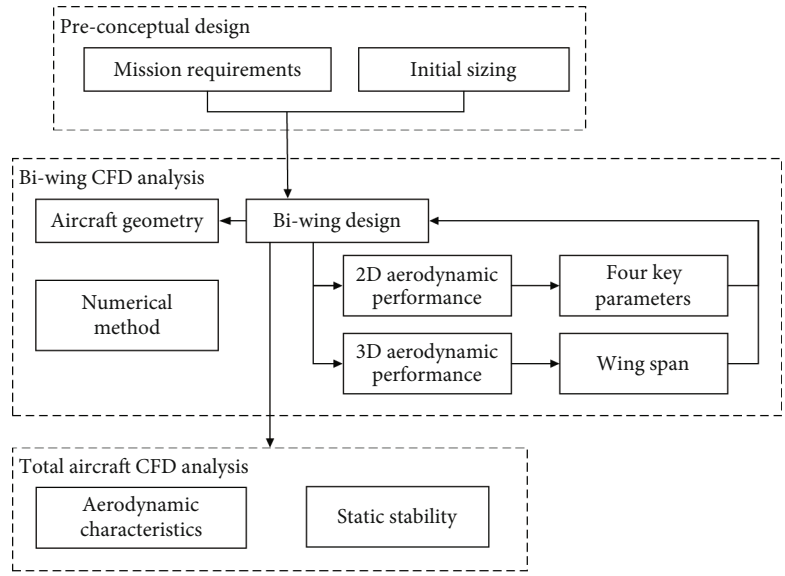

Figure 1: Roadmap of bi-wing study.

High-lift devices (HLDs) are frequently commonly by aircraft designers to enhance lift coefficients. These devices are categorized into two main types: leading-edge high-lift devices (LEHLDs) and trailing-edge high-lift devices (TEHLDs or flaps). LEHLDs improve the wing's stall angle of attack and maximum lift coefficient without causing significant deviations in the wing's lift curve. Often, they are used in tandem with TEHLDs, which also serve to increase the maximum lift coefficient. Together, LEHLDs and TEHLDs alter the airfoil's camber and delay flow separation [10] (pp. 35-113).

However, implementing LEHLDs and TEHLDs in UAVs with short chord lengths presents challenges. The aerodynamic forces exerted by these flaps are borne by structural reinforcement points on the wings, requiring thicker skin to handle the increased torque. An imperfect structural design can compromise wing strength, while the thicker skin can reduce payload weight—a significant drawback for logistics-focused aircraft with high load requirements. The use of two-section or multisection wings can effectively improve lift coefficients without sacrificing wing strength.

In terms of biplane design schemes, Zhang and Ye have studied the aerodynamic characteristics of aircraft with row-type biplane layouts [11]. The research analysed the impact of regular airfoil thickness and hindwing deflection angle on double-tandem wing aerodynamic traits across various angles of attack. Their findings reveal that the tandem wing configuration could delay or even prevent trailing-edge separation, thereby significantly enhancing aerodynamic efficiency. This suggests that such configurations are particularly promising for UAVs. Zhan et al. further investigated biplane configurations aimed at improving the aerodynamic attributes of fixed-wing microair vehicles (MAVs) through low-speed wind tunnel experiments [12]. The study compared the aerodynamic characteristics of various planforms, monoplanes, and biplanes while examining the effects of different gaps, stagger positions, and planform configurations. Based on experimental results, the interaction mechanisms of the flow field were analysed. The study concluded that biplane configurations can indeed improve the aerodynamic characteristics of monoplane fixed-wing MAVs, and that the relative positioning of the biplanes plays a significant role in influencing these aerodynamic attributes.

Several scholars have designed the flap angles in multielement airfoils. Lv et al. [13] used the Reynolds-averaged Navier–Stokes equation to study how various wing and flap angles affect aerodynamic characteristics, specifically employing a DLR-F11 wing for the study. The research identified the optimal flap deflection angle for both takeoff and landing, offering valuable insights for fine-tuning flap control procedures. Similarly, Li et al. [14] focused on a two-section wing, exploring the influence of trailing-edge flap profiles based on specific trainer design requirements. The study investigated how slot size and overlap affect flap lift and surface pressure coefficients. Kong et al. proposed a new trailing-edge lift device based on a large aircraft's basic airfoil to scrutinize the aerodynamic effects brought about by flap bending and spoiler deflection [15]. The study found that downward spoiler deflection enhanced slot airflow, subsequently improving aerodynamic performance. Remarkably, even a slight spoiler deflection could result in significant aerodynamic gains in the linear stage with a small angle of attack.

This paper proposes a twin-boom, inverted V-tailed UAV equipped with a foldable wings configuration [16–18]. The wings of this UAV are designed to adapt to different mission stages; they spread out to provide sufficient lift during takeoff and landing and fold in during cruising to reduce aerodynamic drag. A suitable folding mechanism allows the UAV to transition between these configurations without compromising structural wing strength or flight safety. However, each wing configuration has a unique influence on the flow field. To optimize lift and ensure an

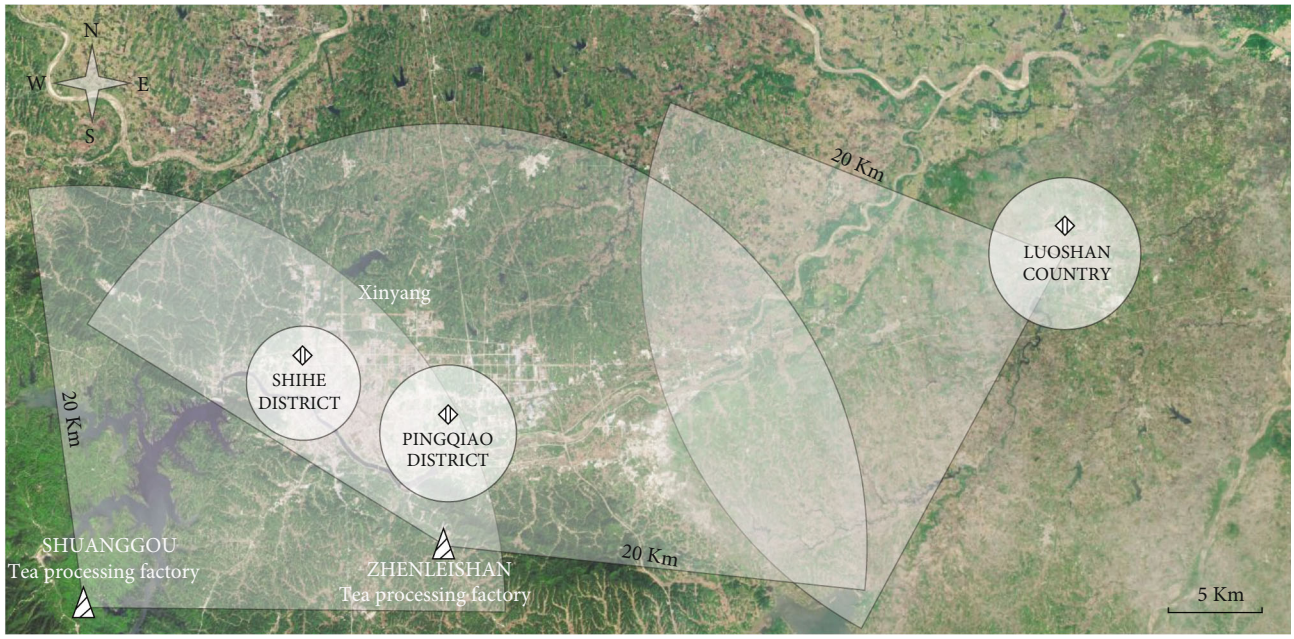

CONVENTIONS

Tea origin

Tea processing factory

Figure 2: Range of UAV operating from the major tea origin is sufficient to serve the entire Xinyang tea-producing area.

CONVENTIONS

Aquatic product base

Aquatic processing factory

Figure 3: Range of UAV operating from major aquatic processing bases and factories is sufficient to serve most Zhoushan fisheries.

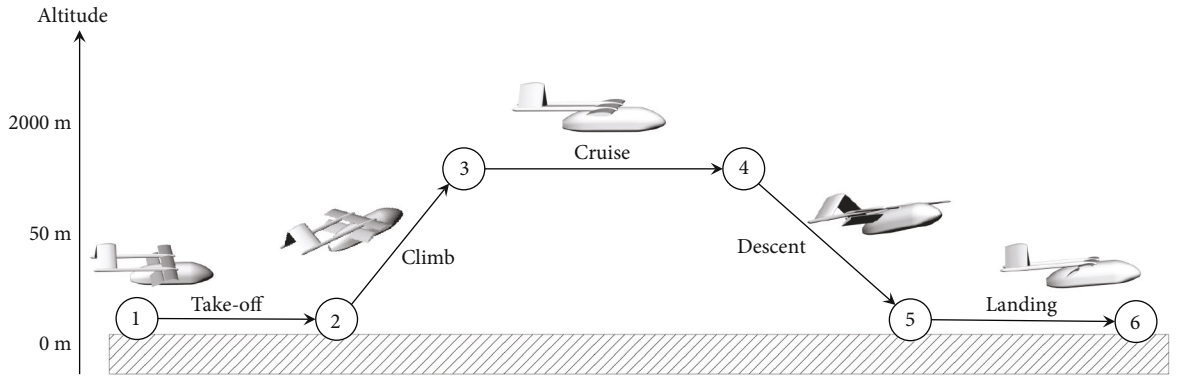

Figure 4: Typical flight profile of UAV.

Table 1: Similar layout UAV-related data statistics.

Aircraft	W_e (kg)	W_0 (kg)	W_p (kg)	W_e/W_0	V_{cruise} (km•h^{-1})	Flight altitude (km)	Flight range (km)
KongJun Z-80 [20]	45	65	20	0.69	180	—	—
XYB H90 [21]	65	90	25	0.72	130	5	200
Hermes90 [22]	75	110	35	0.68	102	5	200
CL-430 [23]	98	128	30	0.77	120	0.98	360
HC-140 [24]	100	150	50	0.67	110	5	—
Crecerelle [22]	110	145	35	0.76	240	4	200
Sojka III-B [22]	115	145	30	0.79	120	4	400
ASN-105 [22]	130	170	40	0.76	90	0.5	10
Phoenix [22]	130	180	50	0.72	157	2.4	140
XYB H180 [25]	150	200	50	0.75	120	5	300

Table 2: Data on three different types of airfoils.

Airfoil section	(t/c) max		Max camber	
	%	%c	%	%c
GA(W)-1 [27]	17	40	2.4	65
NACA0030 [28]	30	30.9	0	0
NACA4412 [29]	12	30	4	40

effective flow field distribution, it is imperative to examine various wing configurations. To end this, this study employed computational fluid dynamics (CFD) for numerical analysis based on this concept.

Figure 1 depicts the research roadmap for this study. The preconceptual design stage involved defining the mission requirements and generating an initial aircraft size and configuration. Guided by pertinent parameters and requirements, the biplane design process was initiated. This design stage is comprised of two-dimensional airfoil design and analysis, as well as three-dimensional bi-wing design and analysis. CFD simulations are employed to compute and assess both the two-dimensional and three-dimensional models. Subsequently, the design parameters for the bi-wing are finalized. The CFD results are then leveraged to evaluate the aerodynamic characteristics and overall stability of the UAV.

The remainder of this paper is structured as follows. Section 2 introduces methodologies employed for the conceptual and preliminary design stages of the UAV. These methodologies encompass weight estimation and aerodynamic design, both aligned with the initial mission requirements. The numerical computational model, including mesh convergence analysis and method validation, is also elaborated. Section 3 delves into the numerical examination of the aerodynamic characteristics based on four key parameters and provides a detailed aerodynamic analysis focusing on the three-dimensional wingspan, aircraft flight performance and static flight stability. The paper concludes with Section 4, summarizing the key findings.

2. Materials and Methods

2.1. Mission Specifications. Mountainous regions and islands are the primary focus for the logistics UAVs in this study, given the unique challenges and mission requirements of these terrains. Constructing long, flat runways in such areas is impractical due to rugged mountainous terrain and the fragmented nature of island groups, which often lack comprehensive road networks. Moreover, these remote locations are often far removed from logistics distribution centres and mainland facilities. Traditional transportation methods such as human portage and trucking are inefficient and inconvenient, while rotorcrafts are ill-suited for carrying large quantities of cargo in areas with variable airflows. In this study, we focussed on using UAVs for the last five-kilometre

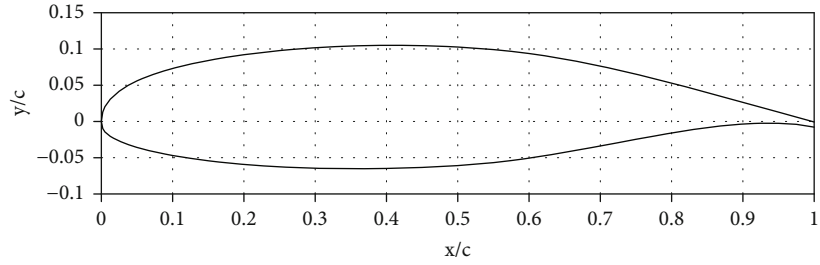

(a) GA(W)-1

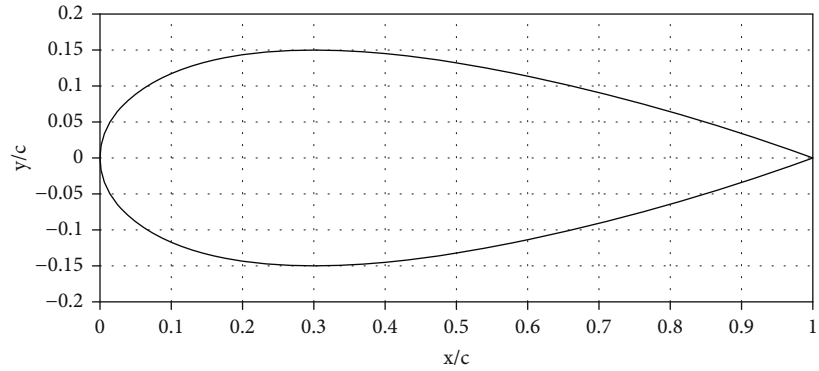

(b) NACA0030

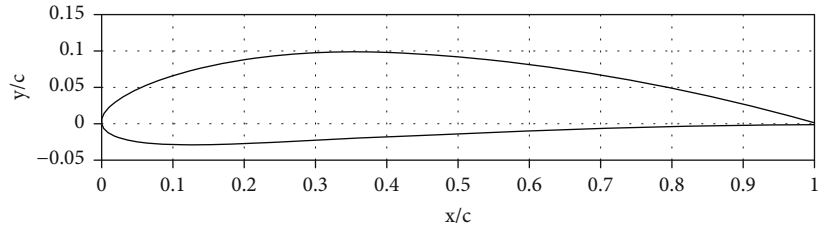

(c) NACA4412

Figure 5: Nondimensional coordinates of three airfoils.

Table 3: Equivalent skin friction drag coefficient.

$C_{D0} = C_{\text{fe}} \frac{S_{\text{wet}}}{S}$	C_{fe}
Net supersonic cruise aircraft	0.0025
Light aircraft (single-engine propeller)	0.0055
Light aircraft (twin-engine propeller)	0.0045
Propeller seaplane	0.0065
Civil logistics aircraft	0.0026

Table 4: Initial UAV geometry parameters.

Parameter	Symbol	Value	Unit
Aspect ratio	AR	7.3	(-)
Wing area	S	1.2	(m^2)
Angle of sweep	Λ	0	(°)
Wing loading	W/S	2435	(N/m^2)
Stall speed	V_{Stall}	13	(m/s)
Maximum sectional lift coefficient	$C_{l\ \max}$	1.6	(-)
Maximum lift coefficient	$C_{L\ \max}$	1.44	(-)
Drag coefficient	C_D	0.044	(-)
Zero-lift drag coefficient	C_{D0}	0.027	(-)
Oswald efficiency	e	0.83	(-)

delivery, aiming to augment mountainous and island-based logistics systems.

To align with these unique geographical constraints, this study conducted a thorough analysis of the flight phases of a logistics UAV to determine the aerodynamic design requirements and objectives.

Two locations in China were selected to represent typical geographical features: Xinyang City in Henan Province, known for its mountainous hills, and Zhoushan City in Zhejiang Province, characterized by its island archipelagos. In Xinyang, the production of Maojian tea is concentrated in mountainous areas, making it difficult for large container vehicles to navigate the region. As a result, tea is usually transported manually, which is both inefficient and poses safety risks. Using rotorcrafts to airlift tea would require significant energy to counteract gravity, making it less efficient for multiple deliveries. Therefore, we considered using logistics UAVs to bridge this gap. By constructing a short runway on a mountain, UAVs can take off and land efficiently,

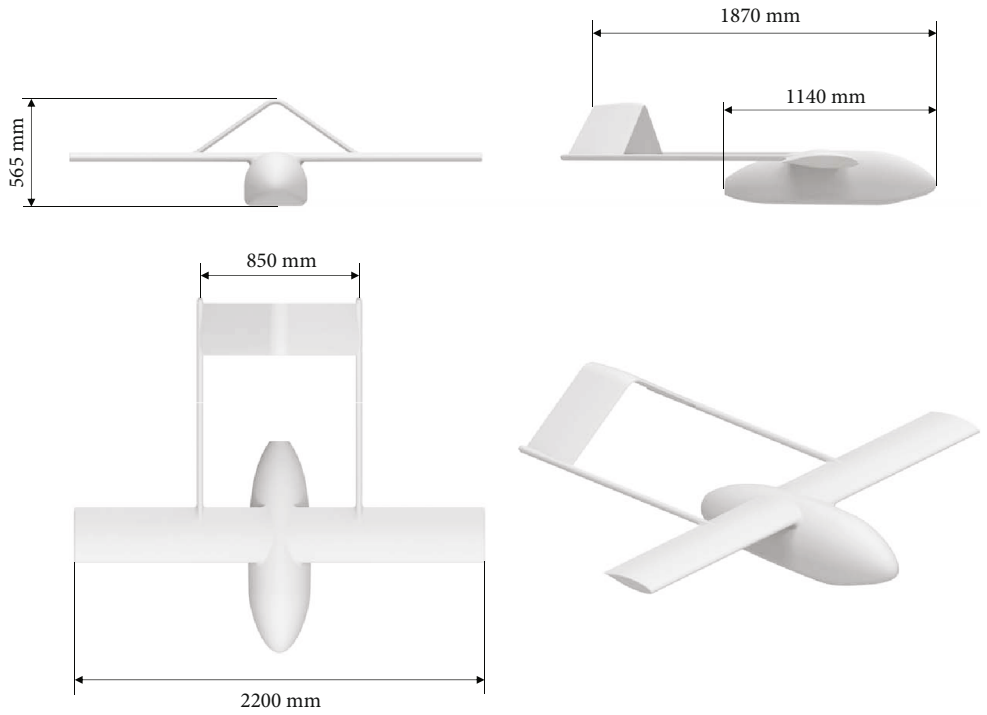

Figure 6: Geometry of the UAV platform.

Table 5: Parameters of the UAV.

Parameters	Value
Wingspan (b)	2.2 (m)
Aspect ratio (AR)	7.3
Cargo volume	80 (L)
Empty weight	57 (kg)
Maximum takeoff weight	82 (kg)
Cruising speed	108 (km/h)

Table 6: Detailed weight breakdown of UAV.

Component	Number	Weight (kg)	Total weight (kg)
Fuselage	1	14.46	14.46
Wing	1	11.26	11.26
V-tail	1	4.82	4.82
Booms	2	0.81	1.62
Avionics	1	12.00	12.00
Engine and propeller	1	3.19	3.19
Batteries	2	4.70	9.40
Electronic governor	1	0.25	0.25
Payload	1	25.00	25.00
		MTOW	82 kg

allowing for a larger cargo capacity and higher aerodynamic efficiency, ultimately reducing the total energy consumption of flights. Employing UAVs for quick, short-distance transport between the tea-picking locations on the mountain and the tea-processing centres at lower elevations could

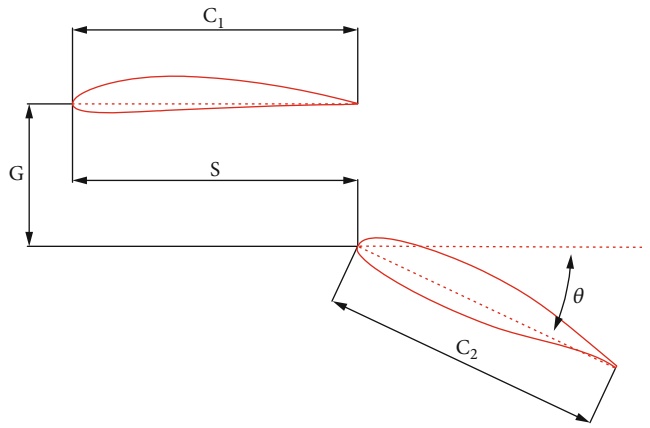

Figure 7: Definitions of bi-wing's chord (C_1, C_2), gap (G), stagger (S), and axes (θ).

streamline the tea industry and significantly reduce labour costs.

For the case study, the UAV was chosen to operate within the airspace of Xinyang. Accordingly, a 40 km round-trip design range was determined to be optimal for covering the major tea-producing areas within Xinyang, such as Shihe, Pingqiao, and Luoshan (as shown in Figure 2). This ensures that the primary tea-producing locations fall within the operational scope of the UAV.

The Zhoushan aquatic product base is a rich source of fresh marine produce that needs to be swiftly transported to various processing points [19]. Given the densely forested and fragmented nature of the Zhoushan Islands, along with scattered fishing locations, traditional ground transportation

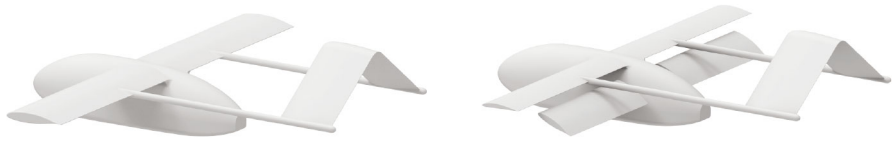

(a) Wings folded during cruise phase (b) Wings unfolded during takeoff and landing phases

Figure 8: Schematic diagram of two configurations.

Table 7: Mesh sensitive study.

No. of computational elements	Lift coefficient	Relative error	Drag coefficient	Relative error
5.64 million	0.1859	—	0.0065	—
11.29 million	0.1814	-2.42%	0.0068	4.62%
22.58 million	0.1822	0.44%	0.0070	2.94%

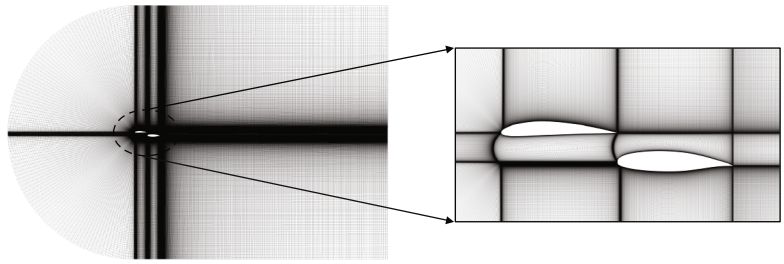

Figure 9: Schematic diagram of two-dimensional bi-wing flow field structured mesh and grid detail.

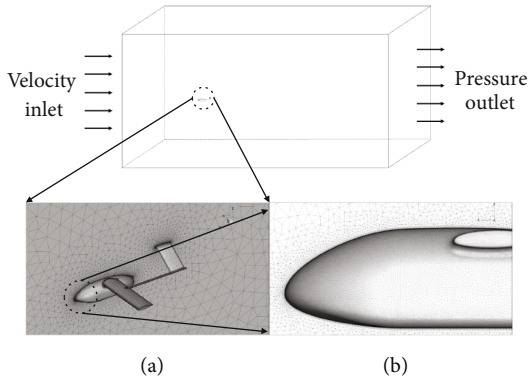

Figure 10: Schematic diagram of three-dimensional UAV flow field and unstructured mesh and grid details. Detailed view of the mesh around UAV (a) and at boundary layer region (b).

is infeasible. Rotorcrafts also face limitations in carrying large quantities of heavy aquatic products. Logistics UAVs, however, are well-suited for quickly moving large volumes of aquatic produce between multiple islands, thus ensuring product freshness. Considering the unique mission requirements for operations in mountainous, hilly, and island terrains, the logistics UAVs must possess essential capabilities such as short takeoff and landing distances, large payload capacities, and excellent cruising aerodynamics. Additionally, these geographical features often present strong convective environments, necessitating a thorough evaluation of UAV stability.

For the case study focusing on the Zhoushan Islands, the UAV is configured for a 40 km operational range, covering major aquatic bases and major fisheries such as Shengshan, Daji, Huangze, Daiqu, Zhougxian, and Jintang (as depicted in Figure 3).

To adapt to different mission requirements, the UAV's aerodynamic configuration can be altered accordingly. Figure 4 illustrates typical flight profiles. During takeoff and landing, the UAV's wings are fully extended to maximize the lift coefficient, facilitating short-distance takeoff and landing. In the cruising phase, the UAV's wings are folded to minimize drag by reducing the aircraft's windward and wetted areas. This enhances the lift-to-drag ratio, extends the flight range, and improved payload capacity.

2.2. Weight Estimation. For initial sizing calculations, Raymer's methodology was employed. The maximum takeoff weight W_0 was then estimated using the following equation:

$$W_0 = W_{\text{pl}} + W_e, \tag{1}$$

where W represents the aircraft weight and the subscripts pl and e correspond to the payload and empty weight, respectively. Equipment such as aircraft power plants and batteries are included in the empty weight category. The UAV's total

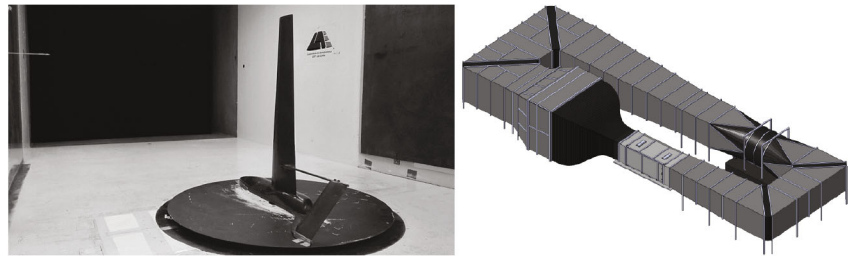

Figure 11: Image of the wind tunnel setup [42, 44].

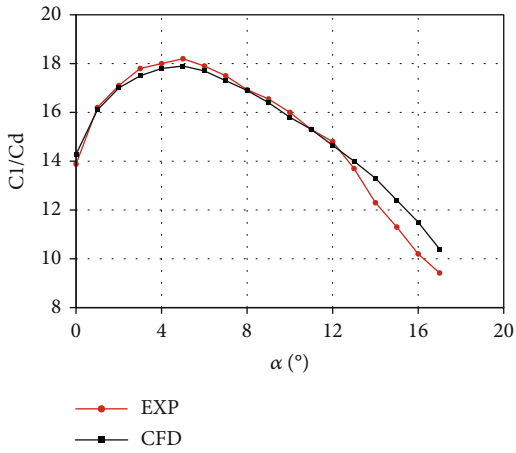

Figure 12: CFD results compared with wind tunnel experimental data [42].

takeoff weight can be expressed using Equation (2):

$$W_0 = \frac{W_{pl}}{1 - (W_e/W_0)} \tag{2}$$

where $(W_e/W_0) = m_e$ denotes the UAV's empty weight coefficient.

The relative empty-to-weight ratio of the total weight engineering empirical formula is $(w_e/w_0) = \mathrm{AW}_0^C K_{\mathrm{VS}}$.

Here, K_{VS} represents the constant for variable sweep value. Given that this UAV has a fixed sweepback configuration, $A = 0.93$, $C = -0.06$, and $K_{\mathrm{VS}} = 1.00$, leading to the UAV's empty-to-weight ratio.

$$\frac{w_e}{w_0} = 0.93 W_0^{-0.06}. \tag{3}$$

Experience statistics on the logarithm of both the takeoff empty weight and the total weight adheres to a linear relationship.

$$\log_{10} W_0 = a + b \bullet \log_{10} W_e. \tag{4}$$

Based on data for similar UAV configurations (shown in Table 1), according to Equation (4), the UAV's total takeoff weight $W_0 = 82$ kg, its empty weight $W_e = 57$ kg, and the empty-to-weight ratio is $(W_0/W_e) = 0.695$.

2.3. Aerodynamic Sizing. Airfoils with a relative thickness of 17% were selected for the GA(W)-1 merge condition. During climb, C_{lmax}, the airfoil's maximum lift coefficient reaches 1.6, and its lift-to-drag ratio (L/D) is 65, based on wind tunnel tests at $R_e = 2 \times 10^6$ and $Ma = 0.15$ [26]. The wings are designed with two configurations, GA(W)-1, NACA0030, and NACA4412, and their specifications are provided in Table 2. Figure 5 shows the nondimensional coordinates of these three airfoils.

Traditional methods for estimating long-wing lift coefficients are based on simplifying wing geometry. By averaging the maximum lift coefficients of the wing root and tip, treating the wing as having a constant airfoil section, and applying a three-dimensional correction, the maximum lift coefficient is obtained using the following equation:

$$C_{L\ \max} = 0.9 \times C_{l\ \max}, \tag{5}$$

where C_{Lmax} is the maximum lift coefficient of the wing.

To calculate the wing area corresponding to the estimated stall speed of 13 m/s, the simplified maximum lift factor is used. The drag coefficient is then determined by assuming that the minimum drag coefficient equals the zero-lift drag coefficient, as expressed in the following equations:

$$C_D = C_{D0} + K_1 C_L^2 = C_{D0} + \frac{C_L^2}{\pi A e}, \tag{6}$$

$$C_{D0} = C_{fe} \frac{S_{\mathrm{wet}}}{S}, \tag{7}$$

where C_D, C_{D0}, S_{wet}, S, and C_{fe} correspond to the drag coefficient, zero-lift drag coefficient, total wetted area of the aircraft, wing reference area, and equivalent skin friction drag coefficient, respectively. As referenced in Table 3, $C_{\mathrm{fe}} = 0.0055$.

This UAV is designed as a transport aircraft with a focus on excellent stall performance. Consequently, it features a straight wing with no sweep angle. Using the straight-wing Oswald efficiency factor,

$$e = 1.78\left(1 - 0.045 AR^{0.68}\right) - 0.64, \tag{8}$$

where e is the Oswald efficiency factor, and AR is the aspect ratio.

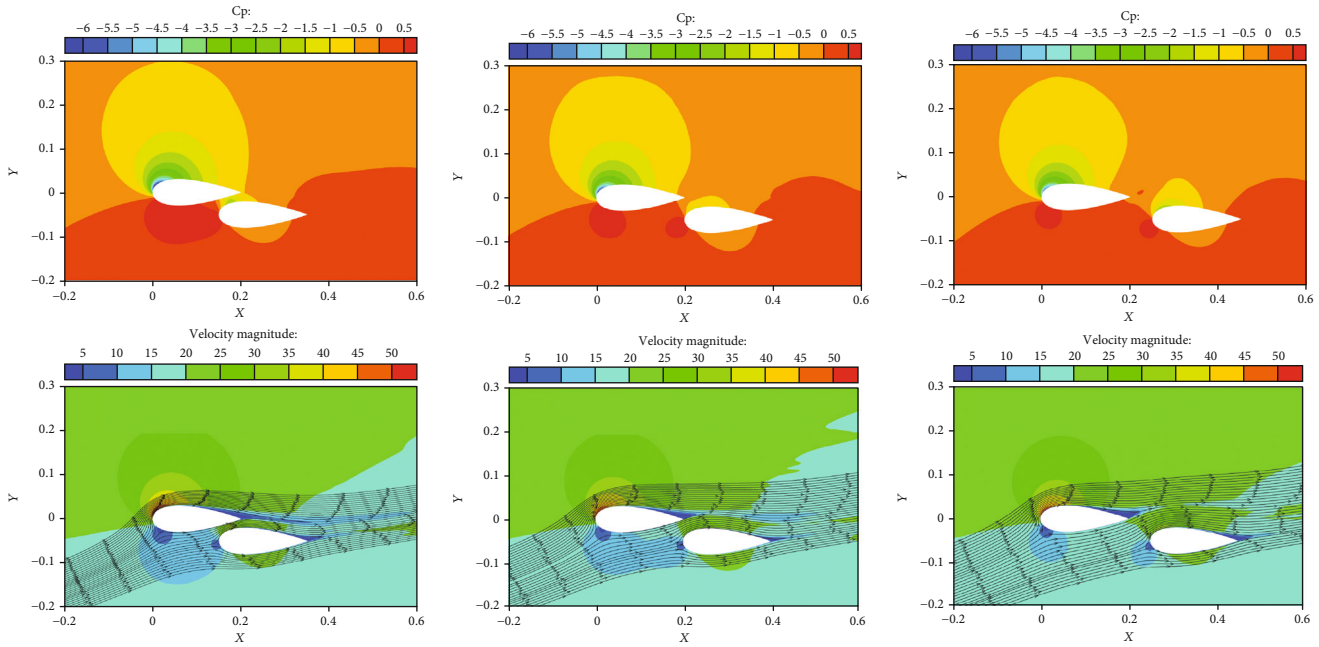

(a) $S = 0.75C$ (b) $S = 1C$ (c) $S = 1.25C$

Figure 13: Sectional flow pressure coefficient, velocity, and vorticity comparison of different S values.

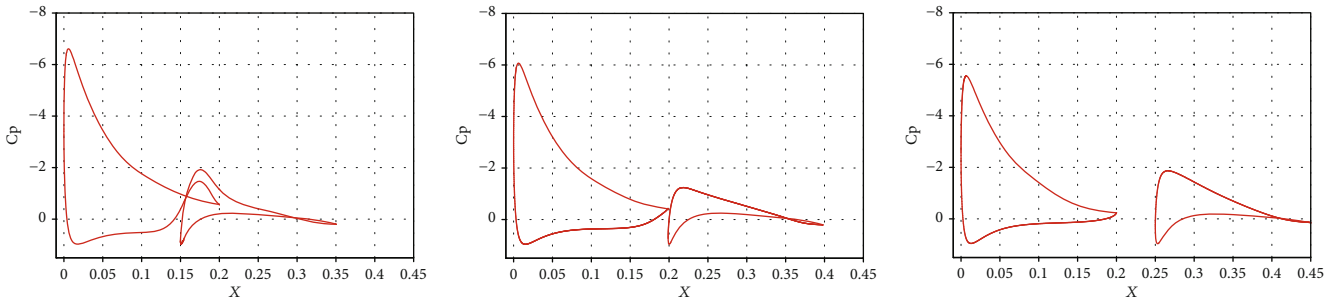

(a) $S = 0.75C$ (b) $S = 1C$ (c) $S = 1.25C$

Figure 14: Sectional pressure coefficient distributions comparison of different S values.

Table 4 summarizes the preliminary estimates for the UAV's geometric dimensions and related parameters.

2.4. Logistics UAV Geometry and Key Design Parameters. Figure 6 illustrates the aircraft's geometry, which incorporates a single straight wing, no dihedral or twist angle, and a twin-boom inverted V-tail configuration [16–18]. Key design parameters are outlined in Table 5, including a sizable takeoff weight of 82 kg and a cruising speed of 108 km/h.

The estimated weights for the primary aerodynamic surfaces and system components are provided in Table 6. The UAV is powered by a GA160 KV67 motor, paired with a 28-inch propeller and an EP-120A-HV electronic speed controller. The total weight of this power unit is approximately 3.44 kg. Energy is supplied by two 12S 27000 mAh batteries from DUPU, weighing 9.4 kg, enabling a cruising flight time of up to 0.8 h at 60% engine power. The aircraft's fuselage, internal frames, and stringers are constructed from aluminium alloy and composite materials. The cargo compartment features a double-layered aluminium cargo skid and a fixed support to accommodate a variety of cargo sizes and weights. Given that the wings and V-tail are responsible for carrying the aircraft's full weight and cargo, they must meet stringent strength and modulus specifications while preserving their original geometric design to achieve the intended aerodynamic performance. The skin and key internal structures, such as the main wing ribs and main spar, are made of aluminium alloy and other materials. Carbon fibre and glass fibre composites are used for the tail boom and other critical connecting components to enhance both economy and repairability. Additionally, the aircraft is equipped with a remote flight control and communication system for defining the mission envelope and for real-time flight monitoring and control.

In traditional lift, large cargo, transport, and general aviation aircraft often utilize leading-edge slats and trailing-edge flaps during takeoff and landing stages to enhance the

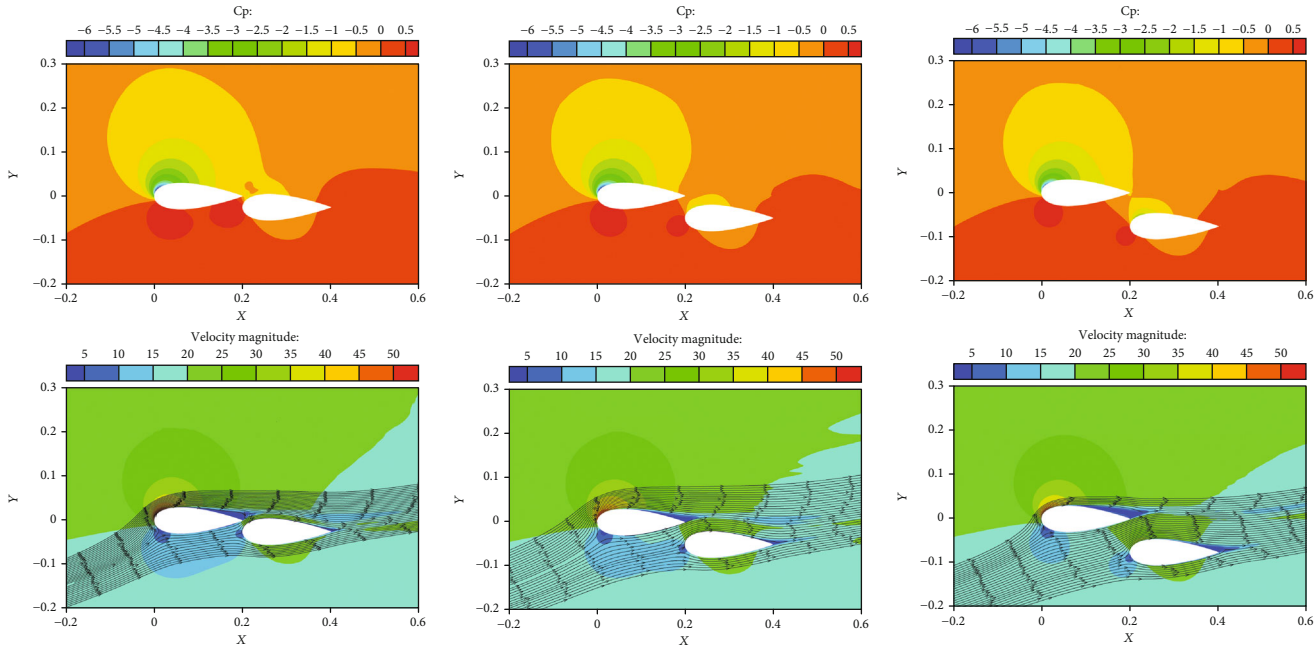

(a) $G = 0.125C$ (b) $G = 0.25C$ (c) $G = 0.375C$

Figure 15: Sectional flow pressure coefficient, velocity, and vorticity comparison of different G values.

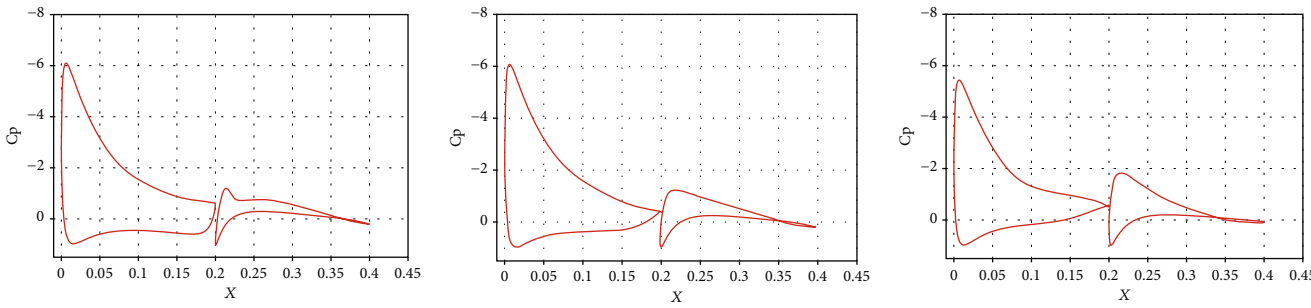

(a) $G = 0.125C$ (b) $G = 0.25C$ (c) $G = 0.375C$

Figure 16: Sectional pressure coefficient distributions comparison of different G values.

lift coefficient. However, the wings of small to medium-sized feeder general aviation UAVs are usually thin with short chord lengths. For larger logistics UAVs, having openings at the front and rear edges compromises wing strength. Additionally, the short chord length makes it challenging to design slat-wing flaps large enough to generate adequate lift. To address these issues, this work introduces a UAV featuring a foldable biplane configuration. The wings spread out during takeoff and landing to maximize lift [6] and fold into a single, integral wing during cruise to minimize drag. The primary focus of this investigation is on how the unfolded wing configuration impacts lift characteristics during takeoff and landing.

Building on existing research on bi-wing configurations [11–13, 30–32], the definitions of the bi-wing elements are illustrated in Figure 7.

In this paper, the terms upper and lower wings are used to describe the two wings of the aircraft. The chord length of the upper wing is denoted by C_1 while C_2 represents the chord length of the lower wing. Both C_1 and C_2 were set at 200 mm based on the results of the conceptual design. S signifies the distance between the leading edges of the upper and lower wings in the direction of incoming airflow, while G indicates the vertical distance between these leading-edge points. θ represents the angle between the axes of the upper and lower wings.

2.5. Foldable Wing Design Schemes. The UAV is engineered with foldable wings; during the cruising phase, the wings integrate into a single-wing form, and during landing and takeoff, they expand into a biplane configuration, facilitated by a specialized folding mechanism. Figure 8 presents models illustrating both wing configurations.

2.6. Numerical Method and Verification. The design calculations set the flow velocity at 30 m/s, with a side slip angle of zero, yielding a project-specific Reynolds number approximately equal to 3.29×10^6 based on the mean aerodynamic

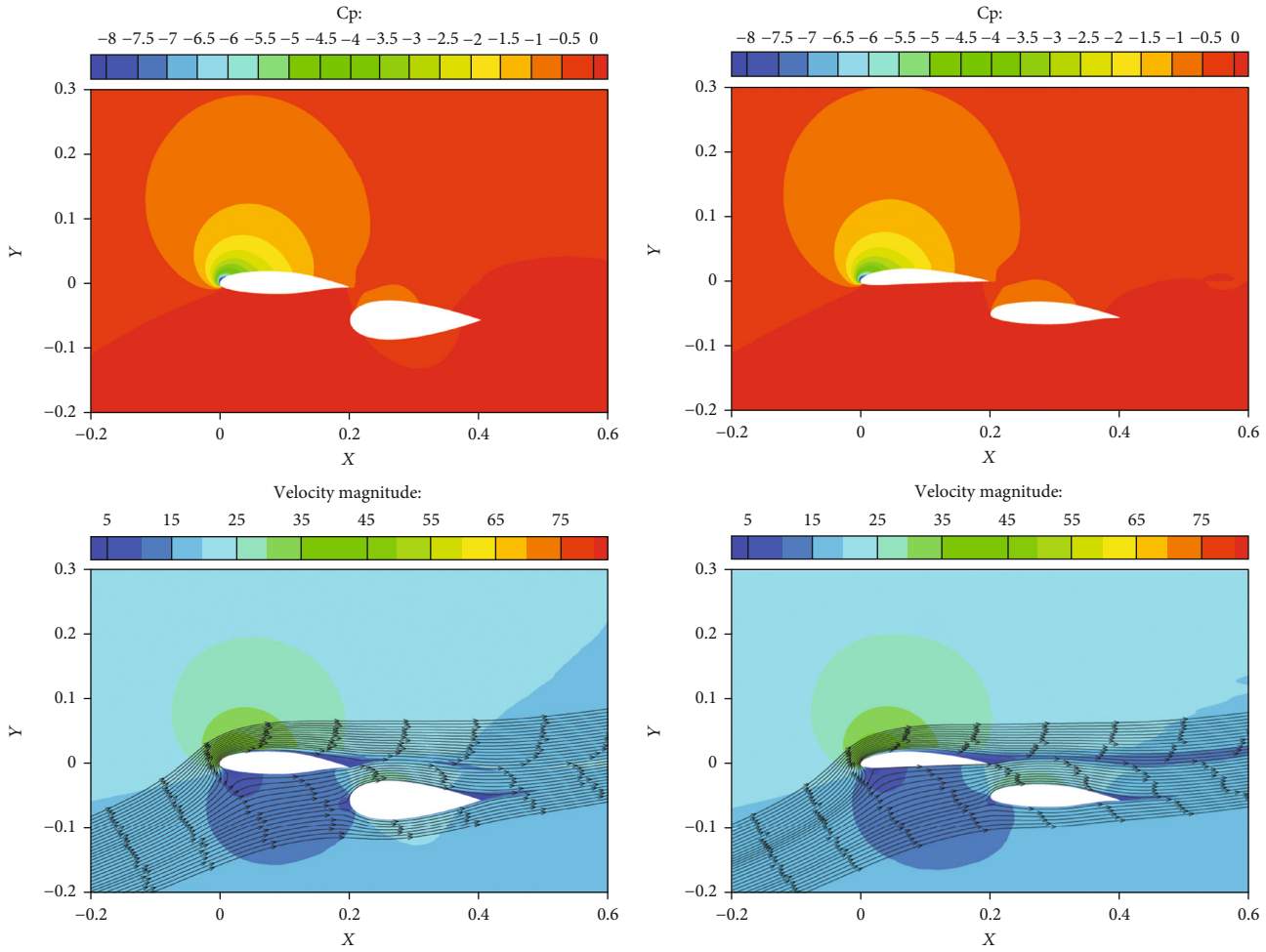

(a) GA(W)-1/NACA0030

(b) NACA4412/GA(W)-1

Figure 17: Sectional flow pressure coefficient, velocity, and vorticity comparison of the two airfoil combinations.

chord (MAC). Computational fluid dynamics simulations were conducted using ANSYS FLUENT with the SST $k-\omega$ turbulence model. The boundary conditions consisted of a far-field velocity inlet and far-field pressure outlet. A second-order upwind discretization scheme was employed to solve the governing equations, and an anisotropic prismatic layer mesh was generated near the object surface. The first layer grid thickness was approximately 10^{-5} the average aerodynamic chord length, with corresponding dimensionless mesh parameters $y_1^+ \approx 1$ [33, 34].

Given that the primary focus is on wing parameters, only the wing was modelled and simulated in this initial study to save computational resources. The complete three-dimensional aerodynamic analysis will follow, based on the derived wing parameters. Two types of meshes were created: a two-dimensional airfoil mesh and a three-dimensional aircraft mesh [35]. During meshing, the effects of far-field boundary conditions were thoroughly considered, and a symmetrical three-dimensional flow field was generated relative to the aircraft's longitudinal profile. To optimize computational time, only half of the geometry was simulated, implementing a symmetry plane along the yz-plane.

The far-field radius for velocity in the two-dimensional quadrilateral mesh was set to be 10 times the model wall's chord length, and the pressure outlet was 20 times the chord length [36–40]. The SIMPLEC algorithm was employed for pressure-velocity coupling. Three levels of mesh density were evaluated, generated by a systematic $\sqrt{2}$ refinement of the reference structured block grid [41]. Aerodynamics coefficients at zero angle of attack were calculated and are presented in Table 7.

Table 6 reveals that the relative errors for the lift and drag coefficients are less than 0.44% and 2.94%, respectively, when the mesh count is between 11.29 million and 22.58 million. Considering both computational accuracy and resource efficiency, the second mesh configuration, with 11.29 million elements, was selected for subsequent two-dimensional calculations and airfoil meshing, as illustrated in Figure 9.

The upstream velocity inlet boundary radius for the three-dimensional tetrahedral mesh was set at 10 times the feature length, while the pressure outlet boundary was 20 times the feature length from the model wall. The pressure and velocity coupling employed the coupled algorithm. The three-dimensional UAV mesh is depicted in Figure 10.

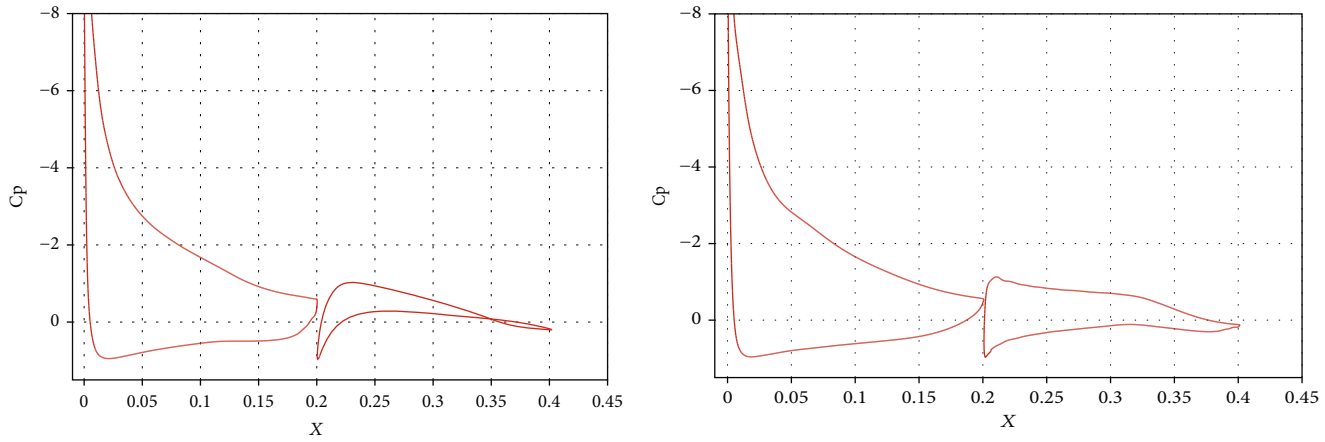

(a) GA(W)-1/NACA0030 (b) NACA4412/GA(W)-1

Figure 18: Sectional pressure coefficient distributions comparison of the two airfoil combinations.

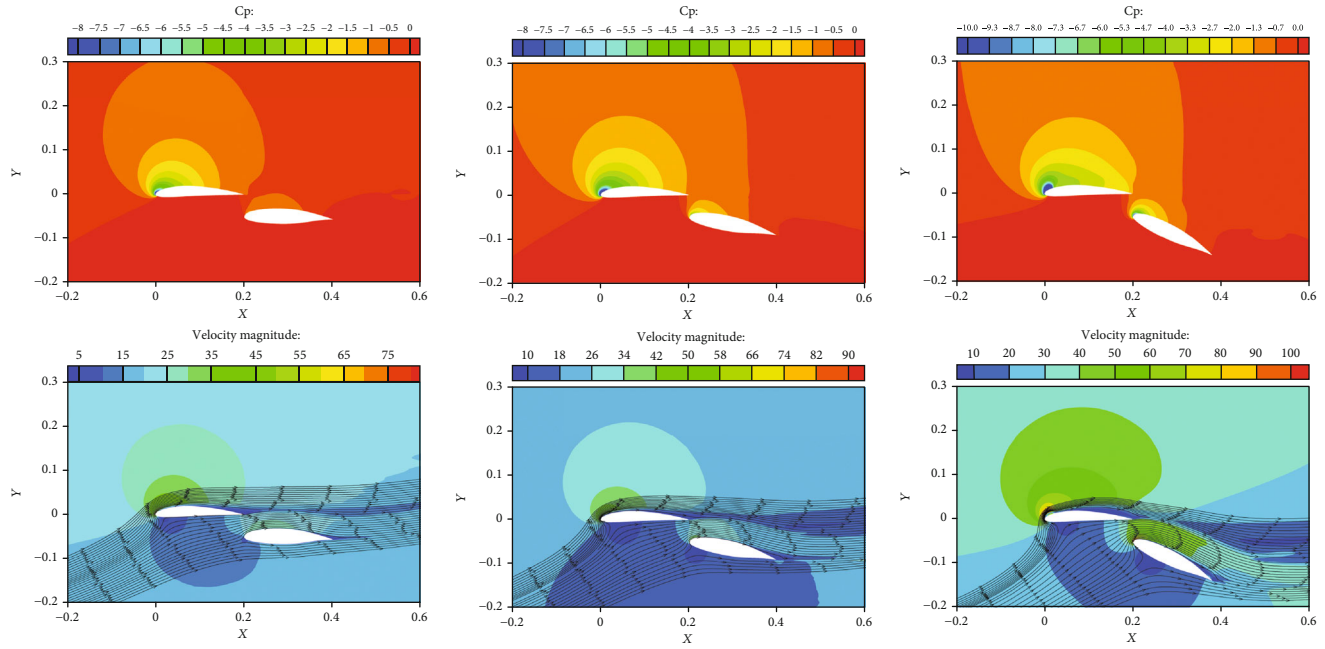

(a) $\theta = 0^{\circ}$ (b) $\theta = 10^{\circ}$ (c) $\theta = 25^{\circ}$

Figure 19: Sectional flow pressure coefficient, velocity, and vorticity comparison of different θ values.

2.7. Numerical Method Validation. The UAV features a high-aspect-ratio, twin-boom inverted V-tail, similar to Bravo-Mosquera's UAV [42]. The computational tool's accuracy was validated by comparing simulation data with wind tunnel experiment results. Key dimensions for Bravo-Mosquera's UAV configuration include a wingspan $b = 2.9$ m, total length $L = 1.6$ m, and MAC = 0.261 m. The incoming flow velocity, determined through CFD simulation, was fixed at 29 m/s, resulting in a Reynolds number 2.97×10^6. Experiments were performed in the LAE-1 closed-circuit wind tunnel at the Aircraft Laboratory of São Carlos Engineering School-University of São Paulo, Brazil (EESC-USP). The LAE-1 wind tunnel was originally designed for automotive tests but is now a multimission facility primarily used for aerospace tests. The tunnel is equipped with an eight-blade fan, driven by a 110 Hp electric motor with seven straighteners located downstream the fan, capable of achieving a maximum speed of 50 m/s with a turbulence level of 0.25% credit due to two 54% porosity screens located before the contraction cone. Instrumentation is composed of a six-component overhead balance, scanivalves and digital pressure scans, and three-channel hot wire anemometer plus 3D traverse gear [43, 44]. The working section has dimensions of 1.29 m in height, 1.67 m in width, and a usable length of 3 m. Atmospheric conditions at the wind tunnel location were recorded as $\rho = 1.079\ \text{kg/m}^3$, $\mu = 1.907 \times 10^{-5}$ Pa s, $T = 24^{\circ}\text{C}$, and $P = 92$ kPa. The aerodynamic balance measures two key forces on the model: lift and drag, with an uncertainty of ±0.01 N. A computational tool in the "Lab View"

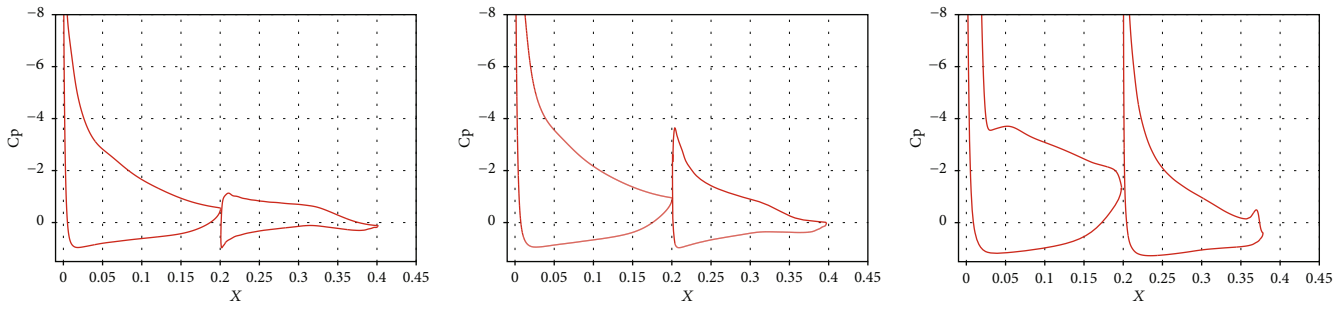

(a) $\theta = 0^{\circ}$ (b) $\theta = 10^{\circ}$ (c) $\theta = 25^{\circ}$

Figure 20: Sectional pressure coefficient distributions comparison of different θ values.

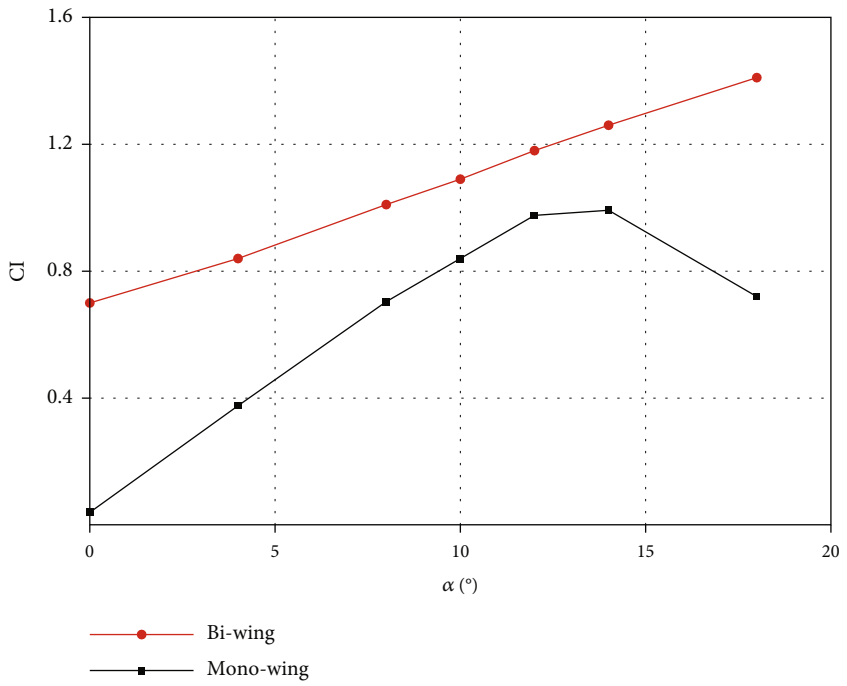

Figure 21: Comparison of lift characteristics of bi-wing and mono-wing.

(National Instrument) program was used, setting to take 5000 samples with a frequency sample of 500 samples per second. The dynamic pressure was measured using a micromanometer with an uncertainty of ±0.1 Pa. Measurement uncertainties of ±0.001 m for chord and wing span, respectively. The experimental uncertainty for each aerodynamic coefficient was thus calculated. $\mu_{C_L} \pm 0.00455$ and $\mu_{C_D} \pm 0.00535$ [45]. The reference URCUNINA-UAV scale model was manufactured by Cliever CL2 Pro Plus 3D printer, using polylactic acid (PLA). Figure 11 shows the model of reference UAV at the wind tunnel test section and its setup [42, 44]. Figure 12 compares the CFD calculations at varying angles of attack with wind tunnel data.

The CFD calculations align well with the wind tunnel experimental data across the studied range of angles of attack [42]. Specifically, the maximum error between the calculated and experimental values before reaching a 13-degree angle of attack is just 2.81%, with an average error of 1.17%. Given these minimal discrepancies and considering the inherent limitations of turbulence models and CFD algorithms when dealing with large angles of attack, both the numerical and experimental methods employed in this study can be deemed highly reliable for future calculations and analysis.

3. Results and Discussion

3.1. Two-Dimensional Aerodynamic Design and Analysis. Compared to its three-dimensional counterpart, a two-dimensional mesh significantly reduces calculation time while still obtaining the influence of the main parameters on aerodynamic characteristics and flow field. Therefore, we initially focus on analysing the flow field around the two-dimensional airfoil [46, 47].

We explored the influence of different variables on the flow field of the wing by changing four key variables: the flow direction distance S, vertical spacing G, angle of the wing

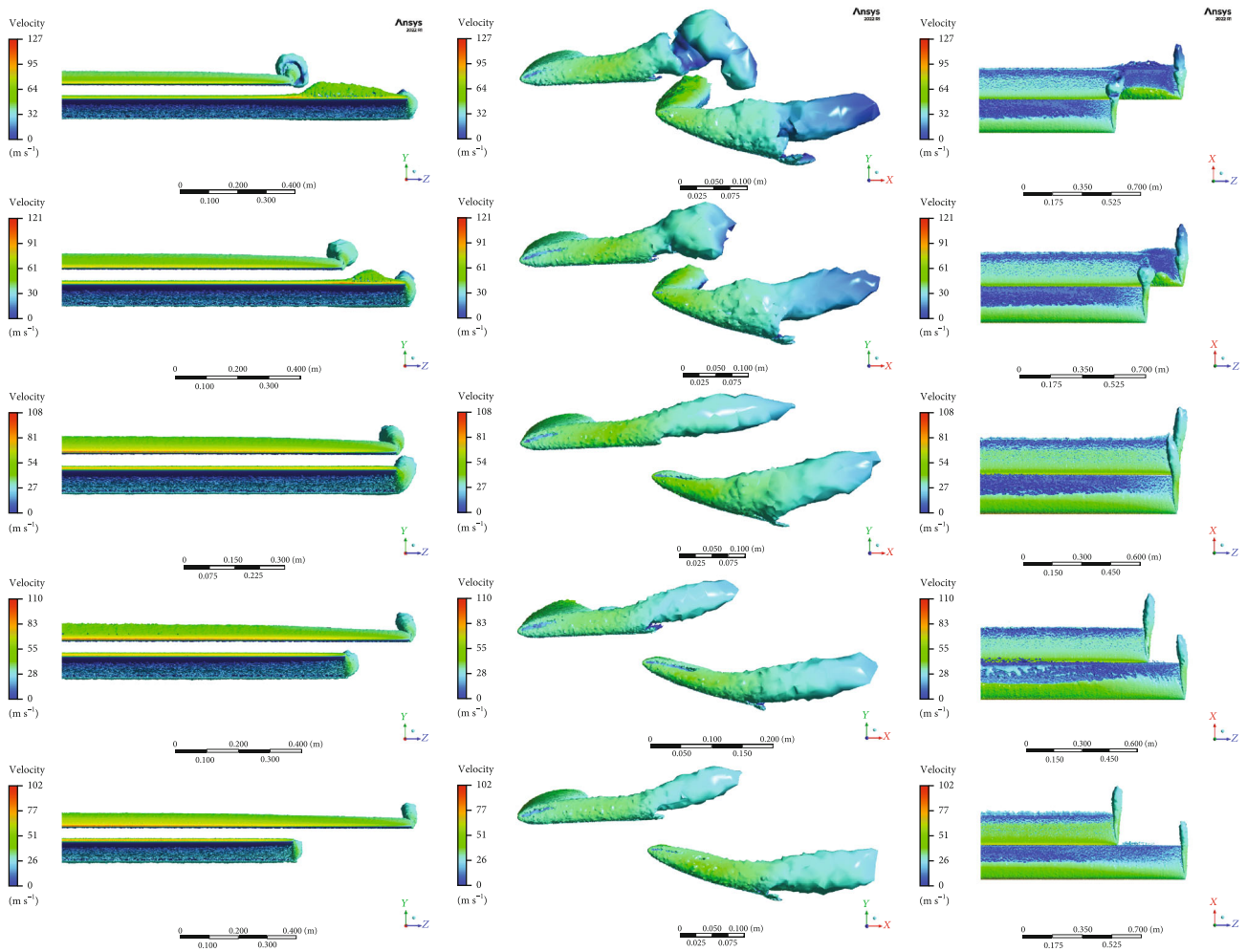

Figure 22: Velocity vortex distribution of five groups of wingspan combinations.

axes θ, and the wing airfoil type [48–51]. The foundational airfoil considered for this paper is NACA0030 [52–54].

3.1.1. Effects of Flow Direction Distance S. Figure 13 compares the pressure contours, stream traces, and vorticity contours at $S = 0.75C$, 1C, and 1.25C. The coefficient of pressure distributions diagram in Figure 14 reveals that when S is less than 1C, the bi-wing gap becomes too narrow. This constriction squeezes the trailing edge of the upper wing, blocking and weakening the high-pressure area and thus causing negative lift. Conversely, when S is greater than 1C, the gap between the wings is too large, diminishing the acceleration of the airflow and the influence of the low-pressure area. This nonuniformity in the high-pressure area adversely affects the upper airfoil, causing airflow separation at the trailing edge. As a result, an S value of 1C was deemed optimal for the incoming flow direction.

3.1.2. Effects of Vertical Spacing G. Figure 15 compares the pressure contours, pathlines, and vorticity contours at $G =$ 0.125C, 0.25C, and 0.375C states. Figure 16 shows the comparison of pressure coefficient distributions between different G values. When the vertical spacing G is less than 0.25C, the gap between the wings is too narrow, obstructing airflow and compromising the low-pressure area of the lower wing. This leads to a flow-blocking bubble and produces a large vortex at the upper wing's trailing edge. Conversely, when the spacing exceeds 0.25C, the gap becomes excessively wide, diminishing the airflow's acceleration in the interwing space and disrupting the low-pressure area of the upper wing. This affects the trailing edge, moves the centre of the low-pressure area forward, exacerbates airflow separation, and weakens the lower wing's lift. Hence, a vertical spacing $G = 0.25C$, i.e., 50 mm is considered more reasonable.

3.1.3. Effects of Different Airfoil Combinations. To maximize lift, airfoils with good aerodynamic performance need to be selected. In this context, the GA(W)-1, NACA4412, and NACA0030 airfoils were evaluated. Figure 17 illustrates the pressure contours, pathlines, and vorticity contours of the upper wing GA(W)-1/lower wing NACA0030, as well as upper wing NACA4412/lower wing

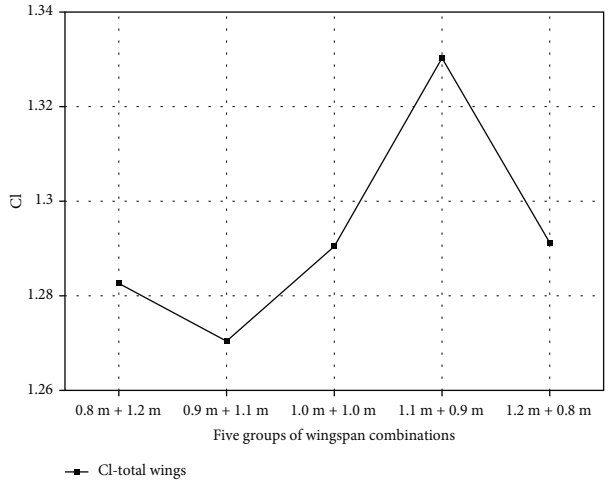

(a) Evolution of lift coefficient of wings among five groups of wingspan combinations

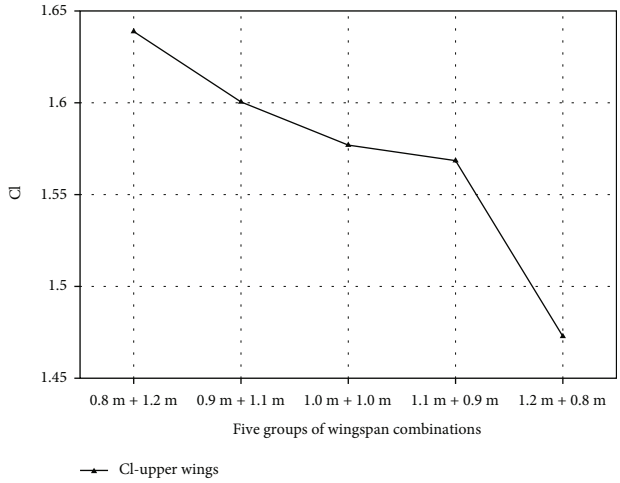

(b) Evolution of lift coefficient of the upper wing among five groups of wingspan combinations

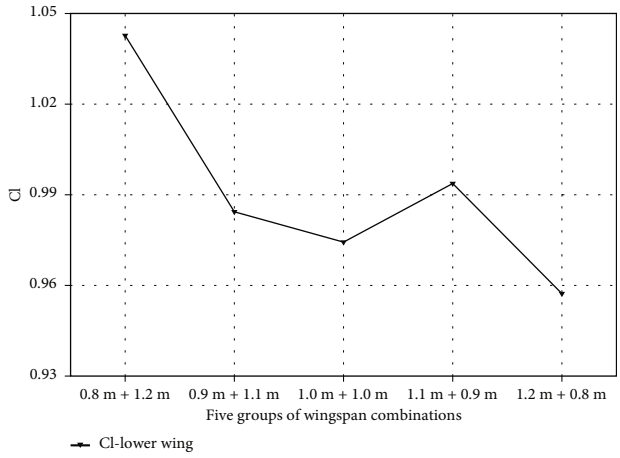

(c) Evolution of lift coefficient of the lower wing among five groups of wingspan combinations

Figure 23: Evolution of lift coefficient of five groups of wingspan combinations.

GA(W)-1 airfoil combinations. Figure 18 shows the comparison of pressure coefficient distributions between the two airfoil combinations.

Analysing the pressure contour and pressure coefficient diagrams (Figure 17) reveals that the upper wing generates more lift than the lower wing. The primary role of the lower wing is to affect the surrounding flow field, change the pressure distribution, and thereby increase the total lift. Our calculations indicate that the lift contribution ratio between the upper and lower wings is approximately 7 : 3. As a result, an

Table 8: Five groups of wingspan combinations' lift coefficient.

Part	0.8 m + 1.2 m	0.9 m + 1.1 m	1.0 m + 1.0 m	1.1 m + 0.9 m	1.2 m + 0.8 m
Upper wing	1.639	1.601	1.577	1.568	1.473
Lower wing	1.043	0.984	0.974	0.994	0.957
Total	1.283	1.270	1.290	1.330	1.291

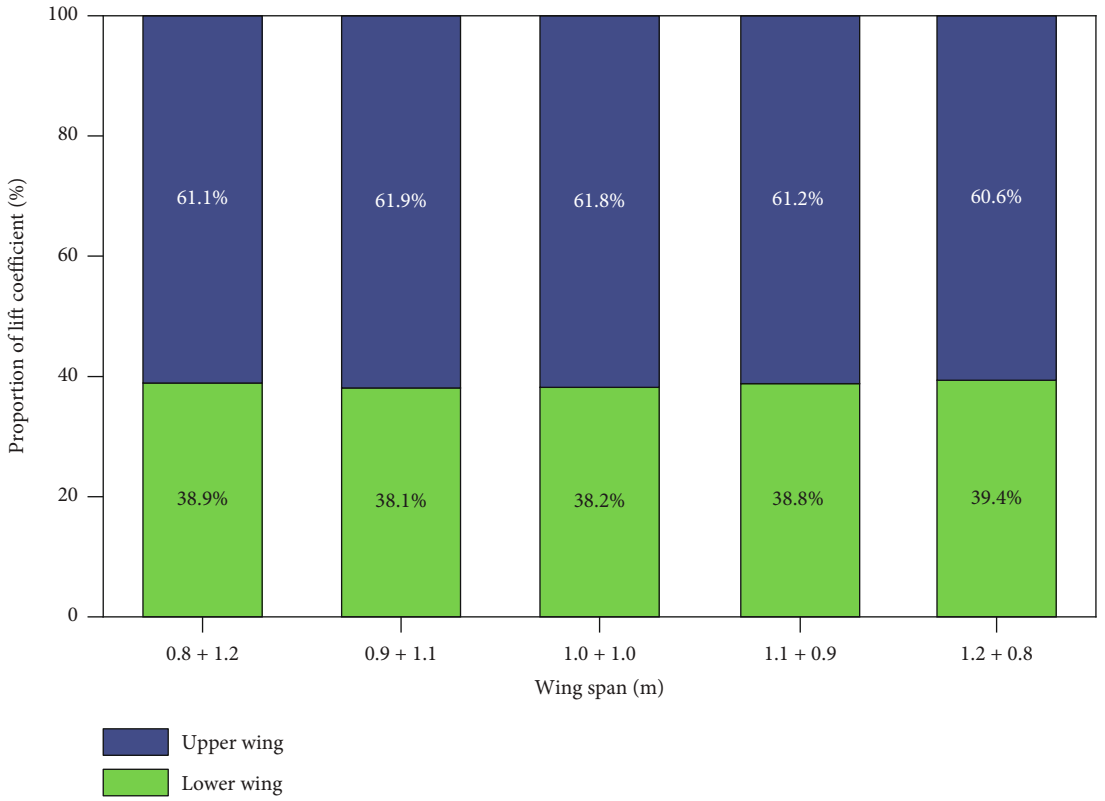

Figure 24: Lift coefficient ratio diagram of five groups of wingspan combinations.

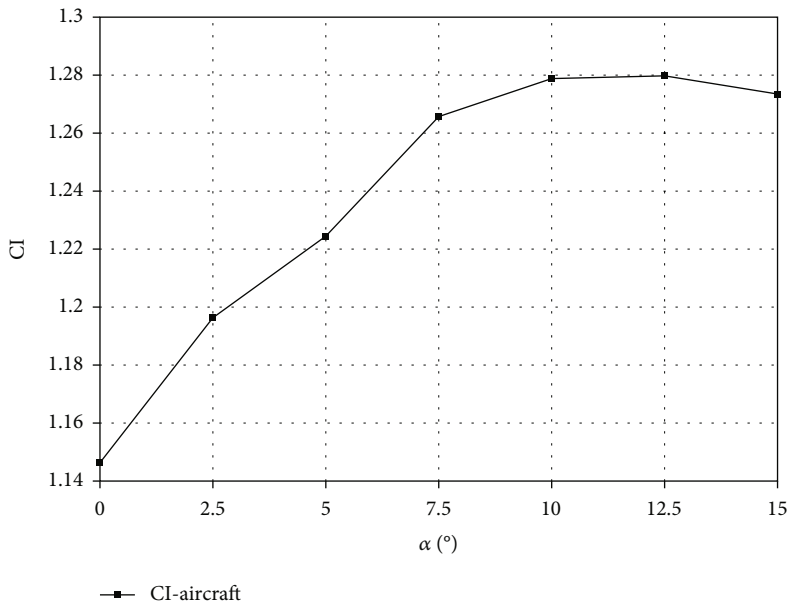

Figure 25: Trends of wings lift coefficient.

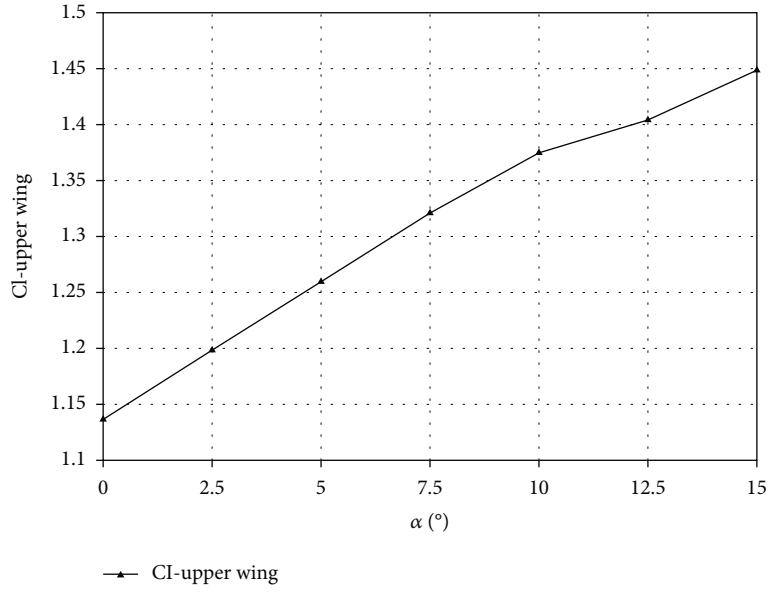

Figure 26: Trends of upper wing lift coefficient.

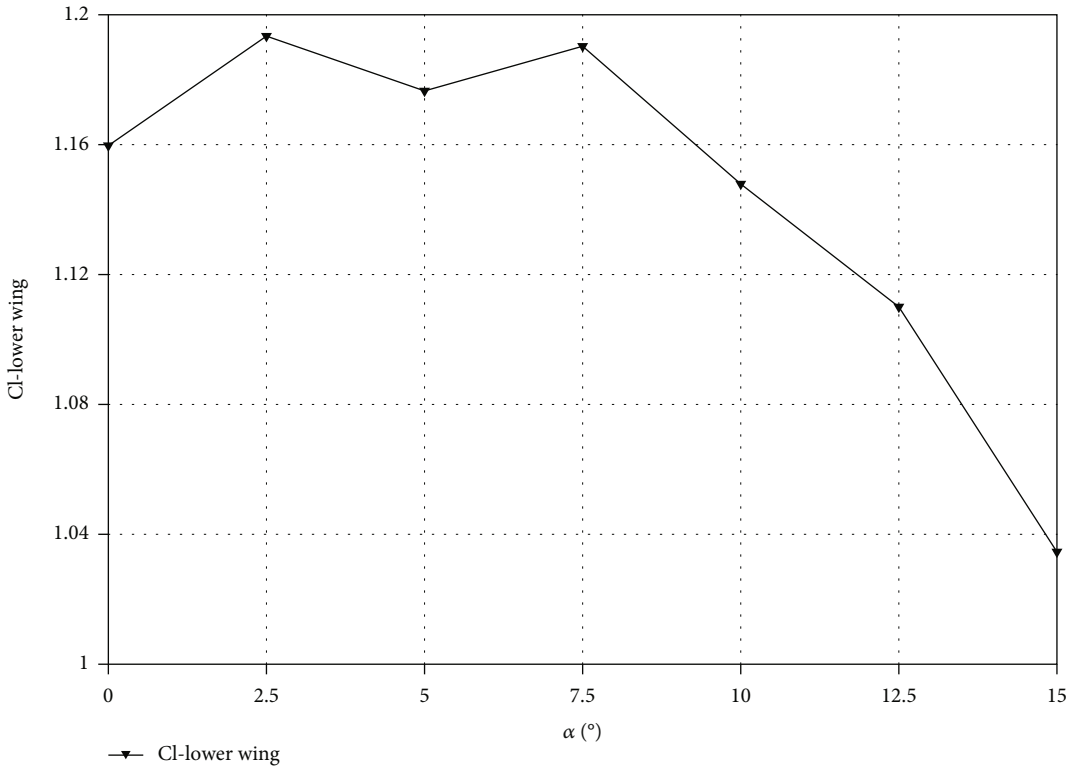

Figure 27: Trends of lower wing lift coefficient.

airfoil with better lift performance should be selected for the upper wing, while the lower wing should feature an airfoil with considerable thickness and a smoother surface. This configuration minimizes lift loss while generating beneficial flow field interference. Accordingly, the upper wing employs the NACA4412 airfoil, and the lower wing employs the GA(W)-1 airfoil.

3.1.4. Effects of Angle θ between Wing Axes. Kong's numerical analysis focused on the aerodynamic properties related to aircraft flap bending and spoilers on the lower wing, while Zhang investigated the aerodynamic characteristics of multisegment wings. Both concluded that a deflection angle of 25–30 degrees on the lower wing of the flap or multisegment wing ensures sufficient lift and a more reasonable flow field

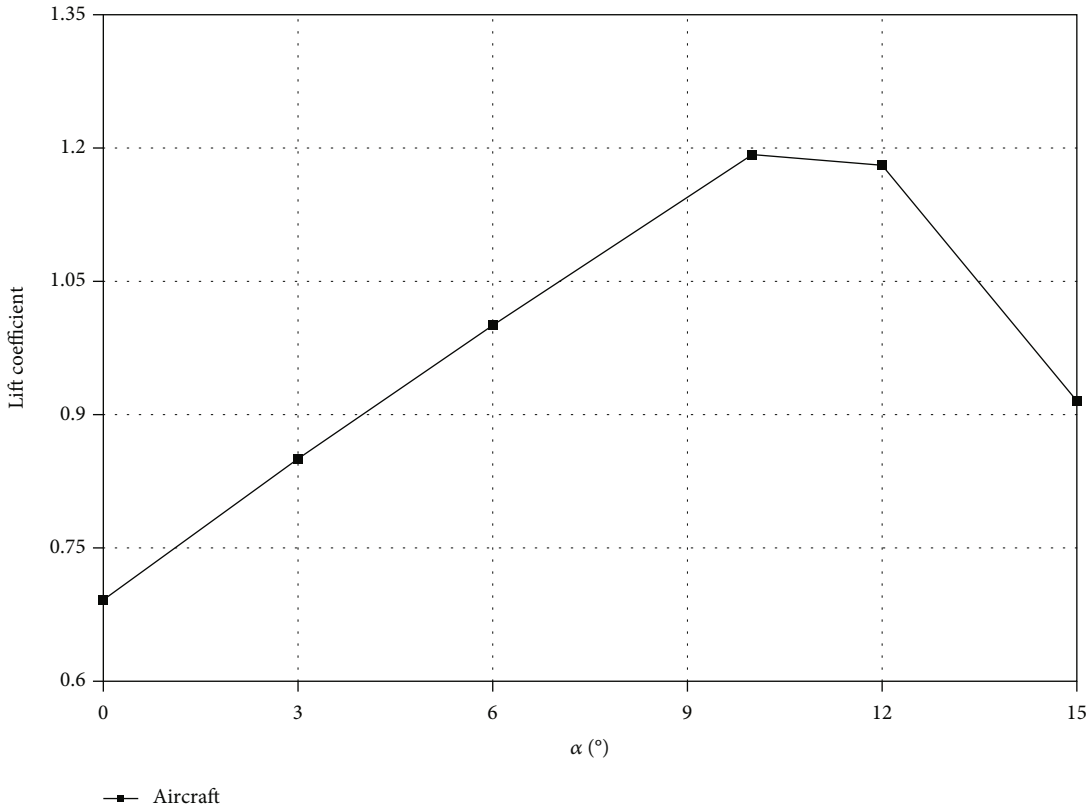

Figure 28: Trends of aircraft's lift coefficient.

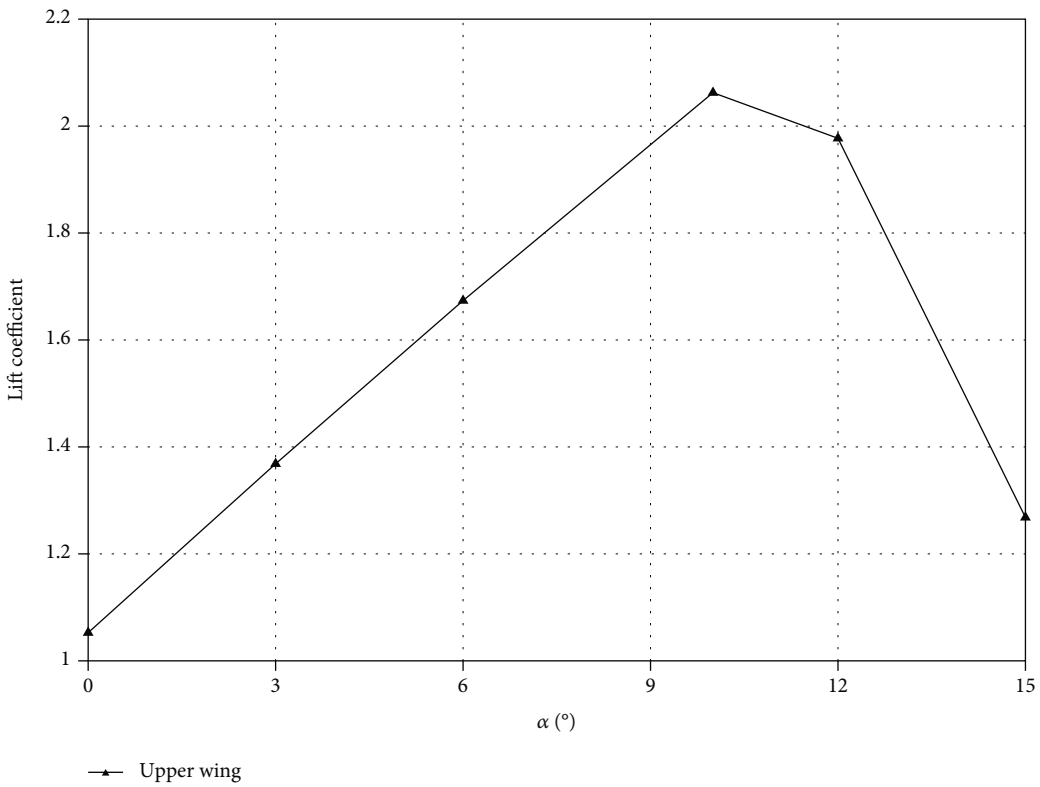

Figure 29: Trends of upper wing lift coefficient.

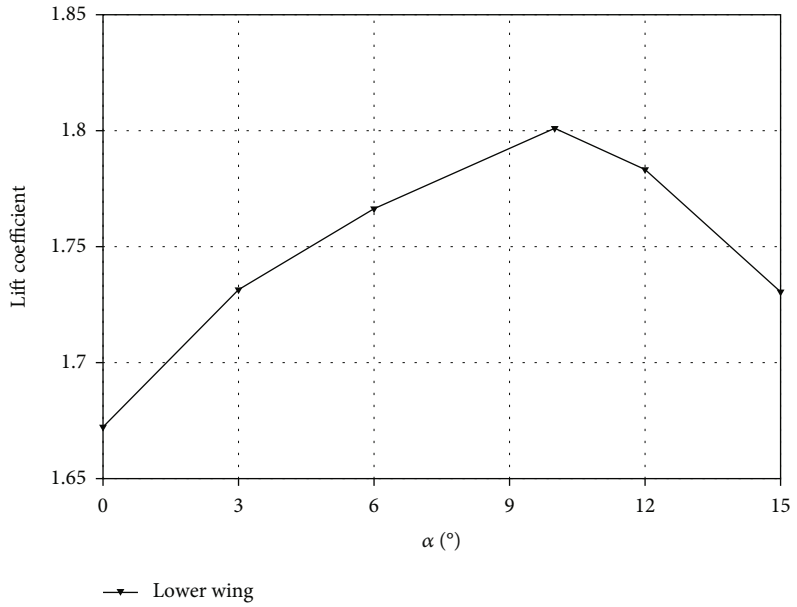

Figure 30: Trends of lower wing lift coefficient.

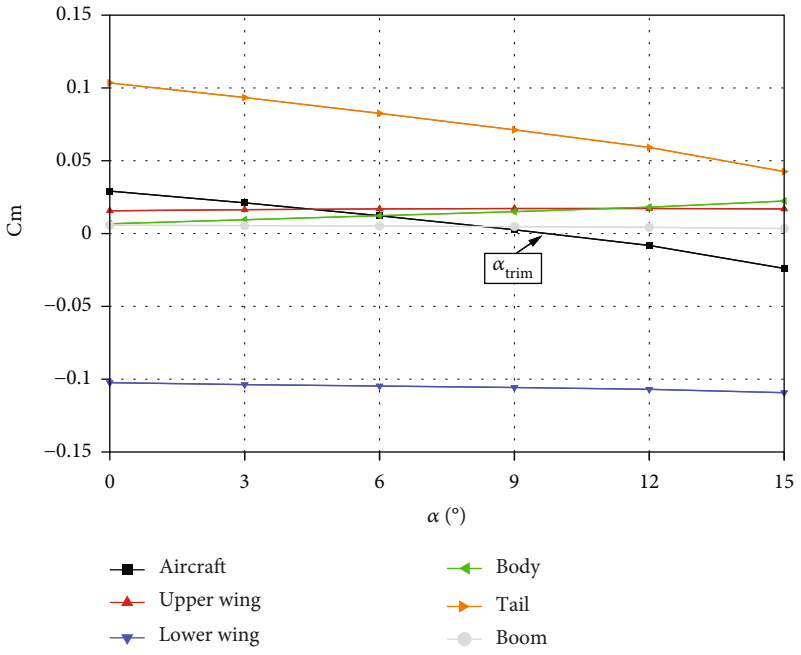

Figure 31: Pitching moment coefficients of the aerodynamic surfaces.

distribution [53, 54]. Based on these findings, three models with different angles—0°, 10°, and 25°—were developed. Figures 19 and 20 depict the calculated pressure contours, pathlines, vorticity contours, and pressure coefficient distributions for these models.

The angle between the two wings' axes critically influences the pressure distribution at the gap opening. At a smaller angle, the gap narrows, severely disrupting the low-pressure distribution of the upper wing surface on the lower wing and preventing an effective pressure differential. Conversely, increasing the angle to 25° yields a more uniform and continuous low-pressure area distribution on both wings, significantly improving the pressure distribution.

Figure 21 depicts the lift characteristic curves for both bi-wing and mono-wing models.

The mono-wing model exhibits pronounced stalling beyond AOA of 14°, while the bi-wing model avoids stalling across all AOAs [55]. Notably, the bi-wing model's lift coefficient surpasses that of the mono-wing model when the AOA is below 10°, providing enhanced lift during the initial takeoff stage and enabling quicker ascents [55–58].

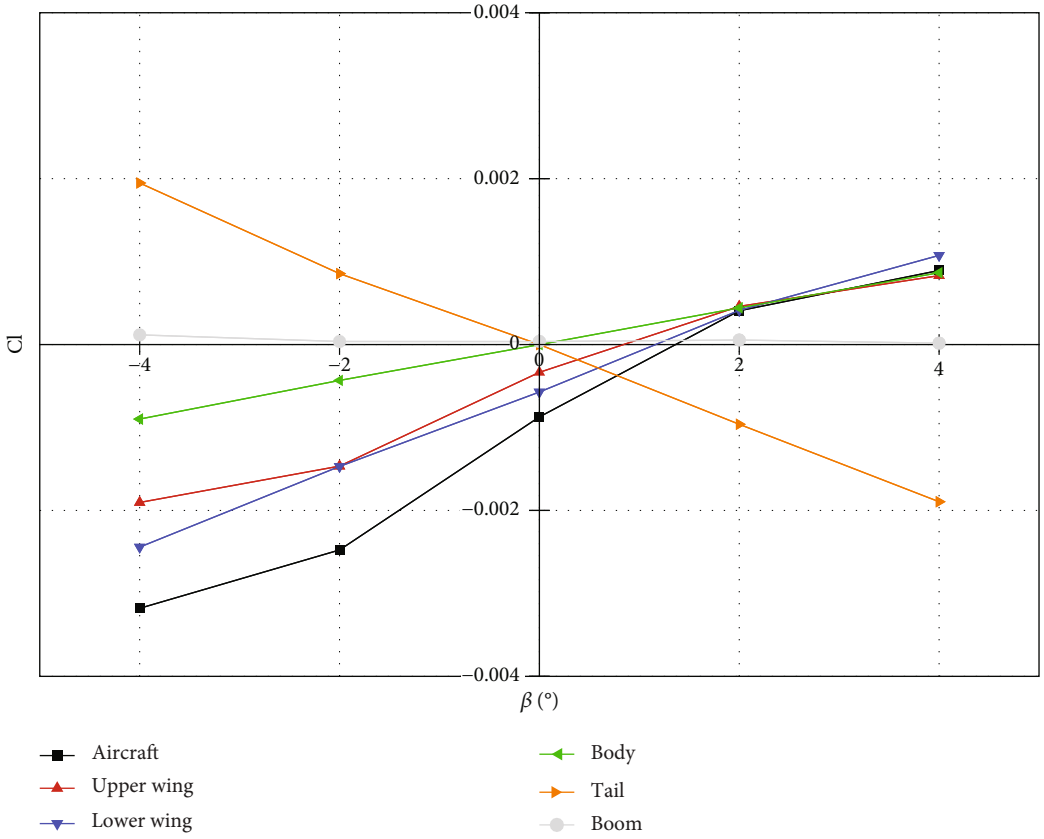

Figure 32: Roll moment coefficients of aerodynamic surfaces.

3.2. Three-Dimensional Aerodynamic Design and Analysis. Based on prior research into two-dimensional bi-wings, the following design parameters were established: $S = 200$ mm, $G = 50$ mm, $\theta = 25°$, NACA4412 airfoil for the upper wing, GA(W)-1 airfoil for the lower wing, and a wingspan of 2 m.

3.2.1. Effects of Different Combinations of Wingspans. Since the two wings together constitute a complete wing system, various bi-wing configurations with different wingspan combinations were analysed. Five typical wingspan configurations were selected for analysis.

Building on a bi-wing span of 1 m + 1 m, the model is designed to maintain a constant projection area on the horizontal, which are 0.8 m + 1.2 m, 0.9 m + 1.1 m, 1.0 m + 1.0 m, 1.1 m + 0.9 m, and 1.2 m + 0.8 m. These five groups of bi-wing models were consistently designed in terms of their two-dimensional sections, meshing protocols, computational environments, and conditions. Figure 22 displays the velocity vortex distribution for these wingspan combinations, and Figure 23 depicts the evolution of the lift coefficient across the five sets.

Figure 22 reveals that as the upper wingspan expands, the wingtip vortices on both wings diminish, along with the vortex interference at the lower wingtip. The lower wing surface in the combination with a shorter upper wingspan showed early vortex separation, as illustrated in the top view of Figure 22(c). A smaller upper wingspan led to increased vortex separation at the lower wingtip. When the upper wingspan surpassed that of the lower wing, the airflow separation between the two wings was suppressed.

Table 8 and Figure 24 list the lift coefficients for various span combinations.

The lift coefficients peaked for an upper wingspan of 1.1 m and a lower wingspan of 0.9 m. As the gap between the wings narrowed, the lift coefficient of the upper wing declined. Specifically, when the upper wingspan was 1.2 m and the lower wingspan was 0.8 m, the narrow gap could not compensate for the lift loss due to leading-edge separation, resulting in a pronounced stall on the upper wing. Figure 24 indicates that the lift ratio between the upper and lower wings consistently hovered around 6 : 4 across the five wingspan sets, explaining the biplane's stall when the upper wingspan exceeded 1.1 m.

Changes in the lower wing's lift coefficient were relatively subdued, making the overall bi-wing lift substantially influenced by the upper wing. Therefore, priority should be given to the lift characteristics of the upper wing. Given the trends in total bi-wing lift and upper wing lift, the optimal wingspan combination was identified as 1.1 m for the upper wing and 0.9 m for the lower wing.

Figures 25–27 showcase the aerodynamic performance for this wingspan combination.

The upper wing, although influenced by the gap, did not experience stalling. The lift coefficient of the lower wing

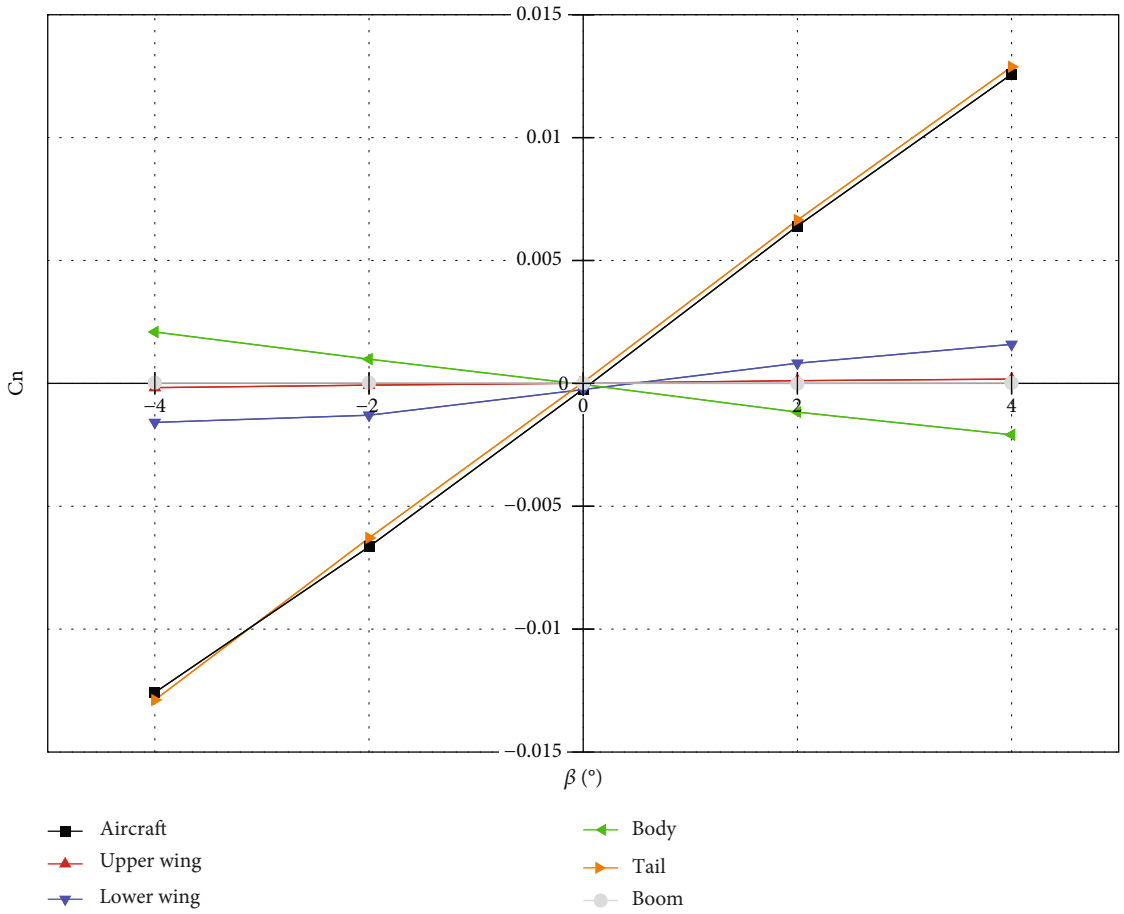

Figure 33: Yaw moment coefficients of aerodynamic surfaces.

Table 9: Stability derivatives of lateral and directional UAV.

Component	$dC_l/d\beta$	$dCn/d\beta$
Body	0.0002	-0.0005
Upper wing	0.0004	0.00004
Lower wing	0.0004	0.0004
Tail	-0.0005	0.0032
Boom	0	0
Aircraft	0.0006	0.0032

started to decline past an angle of attack of 5°; however, the decrease was minimal, and the total lift coefficient reached its apex at an angle of attack of 10°.

3.2.2. Analysis of Aerodynamic Characteristics of UAV. Figures 28–30 present the aerodynamic coefficient curves for both the entire UAV and its bi-wing configuration. During the flight, an expansive continuous low-pressure zone forms between the wing gaps, offsetting lift loss at the upper wing's leading edge and significantly improving its lift coefficient. Due to the 25° angle of attack between the lower wing and incoming airflow when the wings are deployed, the lower wing experiences a higher angle of attack during the fight, thereby exacerbating airflow separation and limiting any lift coefficient increase. However, the bi-wing configuration still yields a higher lift coefficient compared to a two-dimensional airfoil. Throughout the range of flight angles of attack, the UAV maintains a high lift coefficient and only starts to stall at an angle of attack of 12°. This meets the UAV's lift requirements for both takeoff and landing at high angles of attack.

3.2.3. Analysis of Static Stability of Whole UAV. Each component of the UAV contributes to its overall stability, either by influencing its centre of gravity and moment of inertia or by generating aerodynamic forces. The tail, in particular, plays a crucial role in the aircraft's overall stability. A conceptual analysis was conducted to validate the tail design, focusing on longitudinal static stability. The contributions to longitudinal stability from each component were calculated to maintain a constant moment-coefficient derivative. The moment coefficient at the centre of gravity for each component is charted against the angle of attack in Figure 31. Consequently, the trim angle (α_{trim}) for the UAV is established at 10°.

Figure 32 shows the UAV's lateral and directional stability at a 10° angle of attack, displaying the variation curves for both rolling and yaw moment coefficients with respect to yaw angle β. The variations curve of the yaw

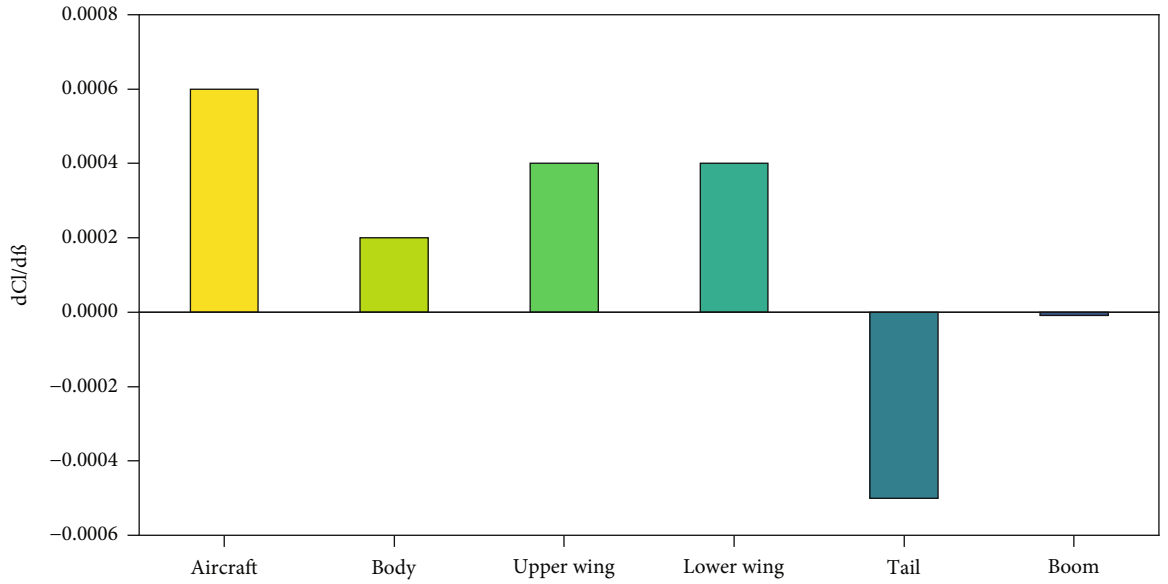

Figure 34: Lateral stability contributions for components of UAV.

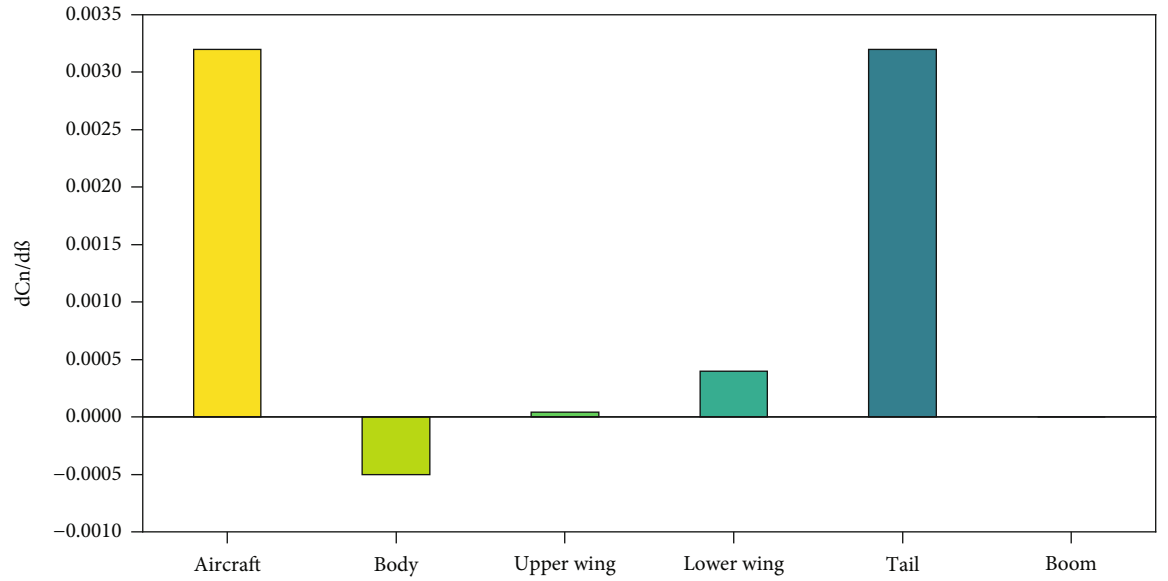

Figure 35: Directional stability contributions for components of UAV.

moment coefficient as a function of the yaw angle β is illustrated in Figure 33, while the static stability derivatives for both lateral and directional stability of the UAV are detailed in Table 9.

Figure 32 reveals that the total UAV's roll moment curve has a positive slope, indicating lateral instability. Figure 33 shows that the yaw moment curve of the total UAV has a positive slope, signifying directional stability.

A deeper examination of each UAV component's effects on lateral and directional stability was conducted, with the results illustrated in Figures 34 and 35. These figures demonstrate that the tail is a significant contributor to the UAV's lateral and directional static stability [59–61].

4. Conclusions

Our study focused on the conceptual design and aerodynamic analysis of a twin-boom, inverted V-tailed UAV with a foldable wing configuration, specifically tailored for the challenging terrains of mountains and islands. We began by reviewing the current state of logistics UAV technology, market demand forecasts, and existing limitations in this field. Given that many mountainous and island regions grapple with inefficient transportation and limited capacity, our research was further motivated to create a UAV capable of meeting varying flight performance requirements across different mission stages. Initially, we conducted an in-

depth analysis of the UAV's mission requirements, which led to a comprehensive aircraft design. This paper consolidates insights and findings from various researchers in the realm of biplane design, proposing a targeted design scheme for our study. Subsequently, we employed reliable CFD methods to scrutinize both two-dimensional and three-dimensional design configurations of the biplane, thereby deriving optimal design parameters. A tailored static stability analysis was also conducted in the context of the UAV's operational environment.

In summary, our aerodynamic analysis elucidated the impact of four critical wing parameters on the wing's flow field. At an incoming flow direction distance S of 1 C, both the high and low pressures on the upper wing surface were too negligible to induce interference, while the high pressure at the lower wing surface near the gap was too dominant to effectively collaborate with the upper wing's low pressure. For vertical spacing G, a value of 0.25 C was found to be optimal. Anything less inhibited airflow acceleration at the gap, whereas a larger value negated the beneficial effects of the gap altogether. An axial wing angle of 25° proved ideal for promoting a large-scale, low-pressure area on the upper wing surface, thereby enhancing the aerodynamic performance of the wing as a whole.

Once the wings are deployed, the aircraft experiences a significant boost in its lift coefficient, meeting the high lift demands necessary for both takeoff and landing. The gap between the wings accelerates the airflow, lowering the pressure behind the gap and directing the airflow on the upper wing surface downward. This not only mitigates separation on the upper wing but virtually eliminates it on the lower wing's upper surface. The result is a uniform pressure distribution across both wings, thereby increasing lift.

Moreover, the interwing gap's acceleration and deflection effects enhance the wing's separation characteristics at high angles of attack. This localized separation only affects the upper wing root and leading edge, allowing the aircraft to maintain sufficient lift. Such attributes improve stall characteristics, ensuring safe takeoffs and landings even on short runways and at high angles of attack.

As for future research avenues, key areas warrant further investigation: Given the evolving complexity of transportation scenarios, drones of various sizes and load capacities should be considered. This calls for a comprehensive analysis of cargo bay loading designs as well as UAV load capacities. Logistics UAVs are subject to rigorous structural strength requirements, necessitating meticulous design and analysis of the aircraft's overall structure. An integrated approach to cargo compartment, load capacity, and structural design can help establish a balanced centre of gravity, thereby enhancing flight stability. Employing multidisciplinary design optimization (MDO) could pave the way for the development of new computational methods, ultimately leading to optimal design solutions.

Data Availability

The data used to support the findings of this study are included within the article.

Conflicts of Interest

The authors declare that they have no conflicts of interest.

Acknowledgments

Funding support is provided by the Science and Technology Project of Henan Province (grant numbers 232102220029, 212102210334, and 202102210267) and the Henan Key Laboratory of General Aviation Technology (grant number ZHKF-230201).

References

[1] S. Lin and B. Zhang, "Research on the future development of UAV logistics distribution industry—Analysis of self-developed new UAV based on Meituan release," *Logistics Engineering and Management*, vol. 5, p. 44, 2022.

[2] J. Grzybowski, K. Latos, and R. Czyba, "Low-cost autonomous UAV-based solutions to package delivery logistics," in *Advanced, Contemporary Control: Proceedings of KKA 2020—The 20th Polish Control Conference*, pp. 500–507, Łódź, Poland, 2020.

[3] X. Hu, B. Pang, F. Dai, and K. Low, "Risk assessment model for UAV cost-effective path planning in urban environments," *IEEE Access*, vol. 8, pp. 150162–150173, 2020.

[4] C. C. Murray and R. Raj, "The multiple flying sidekicks traveling salesman problem: parcel delivery with multiple drones," *Transportation Research Part C: Emerging Technologies*, vol. 110, pp. 368–398, 2020.

[5] S. Li, H. Zhang, Z. Li, and H. Liu, "An air route network planning model of logistics UAV terminal distribution in urban low altitude airspace," *Sustainability*, vol. 13, no. 23, article 13079, 2021.

[6] A. Otto, N. Agatz, J. Campbell, B. Golden, and E. Pesch, "Optimization approaches for civil applications of unmanned aerial vehicles (UAVs) or aerial drones: A survey," *Networks*, vol. 72, no. 4, pp. 411–458, 2018.

[7] V. Szalanczi-Orban and D. Vaczi, "Use of drones in logistics: options in inventory control systems," *Interdisciplinary Description of Complex Systems - INDECS*, vol. 20, no. 3, pp. 295–303, 2022.

[8] L. Kapustina, N. Izakova, E. Makovkina, and M. Khmelkov, "The global drone market: main development trends," *SHS Web of Conferences*, vol. 129, article 11004, 2021.

[9] R. Merkert, M. C. Bliemer, and M. Fayyaz, "Consumer preferences for innovative and traditional last-mile parcel delivery," *International Journal of Physical Distribution & Logistics Management*, vol. 52, no. 3, pp. 261–284, 2022.

[10] M. H. Sadraey, *Design of Unmanned Aerial Systems*, John Wiley & Sons, Southern New Hampshire University, Manchester, NH, USA, 1st edition, 2020.

[11] Q. Zhang and Z. Ye, "Computational investigations for aerodynamic characteristic analysis of low Reynolds number doubly-tandem wing configurations," *Engineering Mechanics*, vol. 36, pp. 244–256, 2019.

[12] H. Zhan, P. Bai, Q. Chen, and Z. Shi, "Experimental investigation on the aerodynamic characteristics of biplane micro-air-vehicles," *Journal of Experiments in Fluid Mechanics*, vol. 23, 2009.

[13] H. Lv, X. Zhang, and J. Kuang, "Numerical simulation of aerodynamic characteristics of multi-element wing with variable flap," *Journal of Physics: Conference Series*, vol. 916, article 012005, 2017.

[14] Z. Li, B. Liang, Z. Liu, X. Jiang, and D. Zhang, "Study on aerodynamic design of 2D flap," *Trainer*, vol. 4, pp. 48–53, 2015.

[15] C. Kong, Q. Qu, P. Liu, Y. Zhai, and Y. Chen, "Numerical study on the deflection of flaps and the partial aerodynamic characteristics under spoiler of large aircraft," in *Proceedings of the 2018 National Conference on Industrial Fluid Mechanics*, pp. 101–108, Beijing, China, 2018.

[16] X. Wang, D. Wu, N. Miao, and Z. Liu, "Aerodynamic performance computations and analysis of a twin-boom configuration airplane," *Flight Dynamics*, vol. 38, pp. 7–10, 2020.

[17] X. Wang, S. Long, D. Wu, and G. Li, "Research progress of general aerodynamic design on twin-boom configuration UAV," *Flight Dynamics*, vol. 39, pp. 1–6, 2021.

[18] S. Suewatanakul, A. Porcarelli, A. Olsson et al., "Conceptual design of a hybrid hydrogen fuel cell/battery blended-wing-body unmanned aerial vehicle—an overview," *Aerospace*, vol. 9, no. 5, p. 275, 2022.

[19] Z. Hu, T. Li, X. Tian, and Y. Wei, "Drone-based emergent distribution of packages to an island from a land base," *Drones*, vol. 7, no. 3, p. 218, 2023.

[20] Kong Jun Z-80http://cn.ttfly.com/com/kongjun/sell/itemid-560.html.

[21] XYB H90http://www.jnxyb.com/proshow.php?id=961.

[22] Y. Zhang, *World Aircraft Handbook, 2011*, Aviation Industry Press, Beijing, China, 2011.

[23] CL-430http://sagetown.com.cn/cn/c/188/p/181.

[24] HONEYCOMB HC-140https://www.hcuav.com/product_detail/72.html.

[25] XYB H180http://www.jnxyb.com/proshow.php?id=962.

[26] S. Gudmundsson, *General Aviation Aircraft Design: Applied Methods and Procedures*, Butterworth-Heinemann, 1st edition, 2013.

[27] GA(W)-1http://airfoiltools.com/airfoil/details?airfoil=ls417-il.

[28] NACA0030http://airfoiltools.com/airfoil/details?airfoil=naca0030-il.

[29] NACA4412http://airfoiltools.com/airfoil/details?airfoil=naca4412-il.

[30] X. Qin, P. Liu, Q. Qu, and G. Peng, "Influence of gap parameters on aerodynamics of multi-element airfoil," *Beijing Hangkong Hangtian Daxue Xuebao/Journal of Beijing University of Aeronautics and Astronautics*, vol. 37, p. 193, 2011.

[31] M. Zhuo, C. Jiang, and C. Li, "Aerodynamic interference between dual wings in transonic box-wing aircraft," *Physics of Gases*, vol. 2, pp. 28–38, 2017.

[32] J.-M. Moschetta and C. Thipyopas, "Optimization of a biplane micro air vehicle," in *Proceedings of the 23rd AIAA Applied Aerodynamics Conference*, p. 4613, Toronto, ON, Canada, 2005.

[33] S. Cheng, Z. Nie, Y. Guo, and X. Zhang, "Influence study of grid topology and turbulence model parameters for multi-element airfoil," *Aeronautical Computing Technique*, vol. 42, pp. 56–59, 2012.

[34] O. Hu and N. Zhao, "Mesh generation and simulation method for 2-D multi-element airfoils," *Aeronautical Computing Technique*, vol. 46, pp. 24–27, 2016.

[35] T. Chen, C. Zhu, and Y. Li, "Analysis of the airfoil aerodynamic performance using CFD," in *Proceedings of the 2nd International Conference on Laser, Optics and Optoelectronic Technology (LOPET 2022)*, pp. 36–50, Qingdao, China, 2022.

[36] J. Huang, Z. Gao, and K. Zhao, "Investigations on low speed flowfield and aerodynamic characteristic of multi-element airfoils," *Flight Dynamics*, vol. 27, pp. 30–32, 2009.

[37] Z. Li, *Aero-Mechanical Optimization Design of a Civil Aircraft's High-Lift System, [M.S. thesis]*, Nanjing University of Aeronautics and Astronautics, Nanjing, China, 2013.

[38] W. Qian and J. Cai, "Numerical simulation of turbulent flow past airfoils at low mach number," *Acta Aeronautica et Astronautica Sinica*, vol. 20, pp. 261–264, 1999.

[39] T. Cebeci, E. Besnard, and H. Chen, "An interactive boundary-layer method for multielement airfoils," *Computers and Fluids*, vol. 27, no. 5-6, pp. 651–661, 1998.

[40] M. F. Ali, N. Khan, W. Akram, and M. O. Qidwai, "Structural design and CFD analysis on airfoil model," *Global Sci-Tech*, vol. 13, no. 2, pp. 64–74, 2021.

[41] C. E. Badoe, Z. Xie, and N. D. Sandham, "Large eddy simulation of a heaving wing on the cusp of transition to turbulence," *Computers and Fluids*, vol. 184, pp. 64–77, 2019.

[42] P. D. Bravo-Mosquera, L. Botero-Bolivar, D. Acevedo-Giraldo, and H. D. Cerón-Muñoz, "Aerodynamic design analysis of a UAV for superficial research of volcanic environments," *Aerospace Science and Technology*, vol. 70, pp. 600–614, 2017.

[43] F. Catalano, "The new closed circuit wind tunnel of the aircraft laboratory of University of Sao Paulo, Brazil," in *24th International Congress of the Aeronautical Sciences*, Yokohama Japan, 2004.

[44] D. Acevedo-Giraldo, "Experimental aeroacoustic and aerodynamic analysis of a large-scale flap side-edge model," in *Proceedings of the 2018 AIAA/CEAS Aeroacoustics Conference*, p. 3799, Atlanta, GA, USA, 2018.

[45] W. H. Rae and A. Pope, *Low-Speed Wind Tunnel Testing*, John Wiley, 1984.

[46] A. E. Ockfen and K. I. Matveev, "Aerodynamic characteristics of NACA 4412 airfoil section with flap in extreme ground effect," *International Journal of Naval Architecture and Ocean Engineering*, vol. 1, no. 1, pp. 1–12, 2009.

[47] Z. Zhu, Y. Chen, Z. Wu, and Z. Chen, "Numerical simulation of high lift system configuration," *Hangkong Xuebao/Acta Aeronautica et Astronautica Sinica*, vol. 26, pp. 257–262, 2005.

[48] S. S. Hariyadi, N. Pambudiyatno, Sutardi, and F. D. P. Fungky, "Aerodynamic characteristics of the wing airfoil NACA 43018 in take-off conditions with slat clearance and flap deflection," in *Recent Advances in Mechanical Engineering: Select Proceedings of ICOME 2021*, pp. 220–229, Singapore, 2022.

[49] L. Hao, Y. Gao, and B. Wei, "Experimental investigation of flow separation control over airfoil by upper surface flap with a gap," *International Journal of Aeronautical and Space Sciences*, vol. 23, no. 5, pp. 859–869, 2022.

[50] J. Watkins and A. Bouferrouk, "The effects of a morphed trailing-edge flap on the aeroacoustic and aerodynamic performance of a 30P30N aerofoil," *Proceedings of the Acoustics, MDPI*, vol. 4, no. 1, pp. 248–267, 2022.

[51] S. Xing, H. Xu, and W. Zhang, "Trailing edge flap effects on dynamic stall vortex and unsteady aerodynamic forces on a pitching airfoil," *International Journal of Aeronautical and Space Sciences*, vol. 2022, article 1674074, pp. 1–20, 2022.

[52] C. P. Van Dam, "The aerodynamic design of multi-element high-lift systems for transport airplanes," *Progress in Aerospace Sciences*, vol. 38, no. 2, pp. 101–144, 2002.

[53] X. Zhang, *Numerical Simulation of Aerodynamic Characteristics of Multi-Element Airfoil, [M.S. thesis]*, College of Air Transportation, Shanghai University of Engineering Science, Shanghai, China, 2017.

[54] Y. Liu, H. Zhu, C. Li, and S. Luo, "Numerical investigation of flow-deflecting gap on controlling flow separation of multi-element airfoil," *Journal of Engineering for Thermal Energy and Power*, vol. 34, pp. 49–56, 2019.

[55] B. Zhang and Z. Lu, "A prediction of the stalling of the multi-element airfoils," *ACAT Aerodynamica Sinica*, vol. 6, pp. 416–425, 1988.

[56] P. Zhang and D. Li, "A lift-enhancing method on multielement airfoil," *Science Technology and Engineering*, vol. 11, pp. 1485–1489, 2011.

[57] R. Zhou, Y. Gao, C. Xiao, Y. Shangguan, and Z. Xi, "Investigation of effect of flap gap on multielement airfoil aerodynamic characteristics," *Journal of Experiments in Fluid Mechanics*, vol. 16, pp. 7–12, 2002.

[58] X. Yang, "Differences between the flow field and aerodynamic characteristics of the lower wing and the upper wing," *Journal of Inner Mongolia University of Technology*, vol. 37, pp. 54–62, 2018.

[59] W. Gong, M. Xia, L. Yue, J. Zheng, and S. Zheng, "Numerical investigation on flow features and static stability characteristics of the V-tail aircraft," *Flight Dynamics*, vol. 39, pp. 19–24, 2021.

[60] Q. Li and Z. Wang, "Investigation of longitudinal moment characteristics of Vee Tail," *Flight Dynamics*, vol. 26, pp. 8–10, 2008.

[61] X. Yang, J. He, and S. Xia, "Analysis of the control characteristics of V-empennage flexible wing aircraft," *Aircraft Design*, vol. 33, pp. 13–16, 2013.